



HAL
open science

Geology of the world-class Kiaka polyphase gold deposit, West African Craton, Burkina Faso

Arnaud Fontaine, Aurélien Eglinger, Koumangdiwè Ada, Anne-Sylvie André-Mayer, Laurie Reisberg, Luc Siebenaller, Elodie Le Mignot, Jérôme Ganne, Marc Poujol

► **To cite this version:**

Arnaud Fontaine, Aurélien Eglinger, Koumangdiwè Ada, Anne-Sylvie André-Mayer, Laurie Reisberg, et al.. Geology of the world-class Kiaka polyphase gold deposit, West African Craton, Burkina Faso. Journal of African Earth Sciences, 2017, 126, pp.96-122. 10.1016/j.jafrearsci.2016.11.017. insu-01397784

HAL Id: insu-01397784

<https://insu.hal.science/insu-01397784>

Submitted on 16 Nov 2016

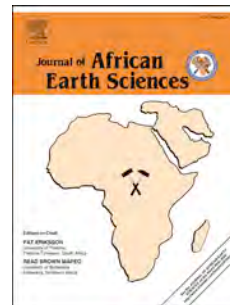
HAL is a multi-disciplinary open access archive for the deposit and dissemination of scientific research documents, whether they are published or not. The documents may come from teaching and research institutions in France or abroad, or from public or private research centers.

L'archive ouverte pluridisciplinaire **HAL**, est destinée au dépôt et à la diffusion de documents scientifiques de niveau recherche, publiés ou non, émanant des établissements d'enseignement et de recherche français ou étrangers, des laboratoires publics ou privés.

Accepted Manuscript

Geology of the world-class Kiaka polyphase gold deposit, West African Craton, Burkina Faso

Arnaud Fontaine, Aurélien Eglinger, Koumangdiwè Ada, Anne-Sylvie André-Mayer, Laurie Reisberg, Luc Siebenaller, Elodie Le Mignot, Jérôme Ganne, Marc Poujol



PII: S1464-343X(16)30374-0

DOI: [10.1016/j.jafrearsci.2016.11.017](https://doi.org/10.1016/j.jafrearsci.2016.11.017)

Reference: AES 2730

To appear in: *Journal of African Earth Sciences*

Received Date: 12 May 2016

Revised Date: 10 November 2016

Accepted Date: 14 November 2016

Please cite this article as: Fontaine, A., Eglinger, A., Ada, K., André-Mayer, A.-S., Reisberg, L., Siebenaller, L., Le Mignot, E., Ganne, J., Poujol, M., Geology of the world-class Kiaka polyphase gold deposit, West African Craton, Burkina Faso, *Journal of African Earth Sciences* (2016), doi: 10.1016/j.jafrearsci.2016.11.017.

This is a PDF file of an unedited manuscript that has been accepted for publication. As a service to our customers we are providing this early version of the manuscript. The manuscript will undergo copyediting, typesetting, and review of the resulting proof before it is published in its final form. Please note that during the production process errors may be discovered which could affect the content, and all legal disclaimers that apply to the journal pertain.

Geology of the world-class Kiaka polyphase gold deposit, West African Craton, Burkina Faso

Arnaud Fontaine^{1,2*}, Aurélien Eglinger^{3,4}, Koumangdiwè Ada⁵, Anne-Sylvie André-Mayer¹, Laurie Reisberg⁶,
Luc Siebenaller^{7,8}, Elodie Le Mignot^{1,6}, Jérôme Ganne⁷, Marc Poujol⁹

¹ GeoRessources, Université de Lorraine-CNRS-CREGU, BP 70239, F-54506, Vandœuvre-lès-Nancy Cedex,
France

² Institut national de la recherche scientifique, 490 rue de la couronne, G1K 9A9, Quebec City, QC, Canada,

³ Center for Exploration Targeting, The University of Western Australia, 35 Stirling Highway, Crawley, Perth,
Western Australia 6009, Australia

⁴ Laboratoire Chrono-environnement, Université de Franche-Comté, UMR CNRS 7249, 16 route de Gray 25030
Besançon, France

⁵ B2Gold Corp. Suite 3100, 595 Burrard Street, PO Box 49143, V7X 1J1, Vancouver, British Columbia, Canada

⁶ Centre de Recherches Pétrographiques et Géochimiques (CRPG), CNRS-Université de Lorraine, 15 rue Notre-
Dame des Pauvres, F-54501 Vandœuvre-lès Nancy, France

⁷ IRD, UR 234, GET, Université Toulouse III, 14 Avenue Edouard Belin, 31400, Toulouse, France

⁸ ONG-D « Le Soleil dans la Main » asbl, 48, Duerfstrooss, L-9696 Winseler, Luxembourg

⁹ Géosciences Rennes, UMR CNRS 6118, OSUR, Université de Rennes 1, 35042, Rennes Cedex, France

*Corresponding author:

Arnaud Fontaine

Centre Eau Terre Environnement

Institut national de la recherche scientifique

490, rue de la couronne, G1K 9A9, Quebec city, CANADA

E-mail: arnaud.fontaine@ete.inrs.ca

Keywords: orogenic gold deposit, Eburnean orogeny, metamorphism, magmatism, Birimian volcano-
sedimentary belt, U-Pb and Re-Os geochronology

30 **Abstract**

31

32 The Kiaka gold deposit is a major resource in West Africa, with measured and indicated resources of 124 Mt at
33 1.09 g/t Au (3.9 Moz) and inferred resources of 27 Mt at 0.83 g/t Au (0.8 Moz). Located within the Manga-Fada
34 N’Gourma greenstone and plutonic belt in south of the Burkina Faso, the deposit is hosted by a metamorphosed
35 volcano-sedimentary sequence of lithic-, quartz-biotite metagreywacke, aluminosilicate-bearing metapelites and
36 garnet-orthopyroxene-bearing schists and volcanic units.

37 Structural observations indicate four local deformation events: DK₁, DK₂ and DK₃ and DK₄. Respectively, these
38 events are linked to regional D₁ E-W compression, D₂ NW-SE compression and lastly, D₃- and D₄-related
39 reactivations along D₂ shear zones. The S₂ foliation and D₂-related shear zones are developed during lower
40 amphibolite facies metamorphism whereas retrogression occurs during D_{3,4} reactivations along these shear zones
41 at upper greenschist facies conditions. The emplacement of a dioritic intrusion, dated at 2140 ± 7 Ma (Concordia
42 U-Pb age on magmatic zircon), is interpreted to be contemporaneous with sinistral displacement along
43 mineralized, NE-trending D₂ shear zones. The intersection of these shears zones and the Markoye shear zone
44 (dextral-reverse D₁ and sinistral-reverse D₂ reactivations) controlled the final geometry of the host rocks and the
45 ore zones.

46 Four subparallel elongated ore bodies are mainly hosted within D₂-related shear zones and some are developed
47 in an apparent axial plane of a F₂ isoclinal fold. Detailed petrographic studies have identified two main types of
48 hydrothermal alteration associated with two stages of gold mineralization. The stage (1) corresponds to
49 replacement zones with biotite and clinozoisite during the D₂ event associated with pyrrhotite ± pyrite,
50 chalcopyrite (disseminated gold stage). The stage (2) occurs during reactivations of the D₂-related auriferous
51 shear zones (vein stage) and are characterized by diopside ± actinolite D₃ veins and veinlets and D₄ pervasive
52 muscovite, ± chlorite, ± calcite in quartz-carbonate vein selvages and associated with pyrrhotite + arsenopyrite ±
53 electrum, ± native gold and tellurobismuthite. The latter stage (2) could be divided into two sub-stages based on
54 mineralogy and crosscutting relationship. A weighted average Re-Os pyrrhotite age at 2157 ± 24 Ma (Re-Os age
55 based on 3 replicates) constrains the timing of the disseminated gold stage and represents the first absolute age
56 for gold mineralization in the Manga Fada N’Gourma area. The timing of gold at Kiaka may be also coeval with
57 one of the two lode gold event at ~ca. 2.16-2.15 Ga and occurred concomitant with tectono-thermal activity
58 during Eo-Eburnean orogeny.

59 The study of the Kiaka gold deposit emphasizes the importance of a multi-scale and multidisciplinary approach
60 (field observations, petrography geothermobarometry and geochronology) to decipher the polyphase character of
61 some Paleoproterozoic gold deposits.

62

63 **Introduction**

64

65 Orogenic gold deposits represent a major source for global gold production (Goldfarb et al. 2001, Frimmel,
66 2008). These ore deposits formed from the Paleoproterozoic (gold mineralization in the Pilbara craton dated at ca.
67 3.4-3.3 Ga; Neumayr et al. 1998) to the early Cenozoic (gold-bearing quartz veins in the Southern Alps formed
68 during the last 7 Ma; Craw and Koons 1989). The term “orogenic” is linked to their close association with
69 accretionary and collisional orogens (Groves et al., 1998). Ore in such deposits is (i) epigenetic and hosted by
70 deformed and variably metamorphosed rocks at mid- to shallow crustal levels (Böhlke 1982; Goldfarb et al.
71 2001, 2005), (ii) spatially associated with major crustal structures (Sibson et al. 1988; Colvine et al. 1988;
72 Kerrich et al. 2000). Some authors have also argued for a spatial and/or temporal association between gold and
73 granitoids of variable composition (Colvine et al. 1988; Champion and Sheraton 1997; Cassidy et al. 2002;
74 Goldfarb et al. 2005; Doublier et al. 2014). The relationship between gold and magmatism is probably due to the
75 the late-orogenic extensional tectonics that also focuses plutonism along auriferous structures. Granites can also
76 provide thermal perturbations, competence contrasts at belt to deposit scale and/or may also contribute some
77 metals and/or ligands that are district specific (Wyman et al., 2016).

78

79 Crustal scale processes are invoked for the formation of orogenic gold systems (McCuaig and Hornsby, 2014;
80 Wyman et al., 2016) as they form in a very short time in relation with tectonic triggers, controlling the transfer of
81 fluids within the crust (Sibson et al., 1988; Cox, 2005; Weatherley and Henley, 2013). They are products of
82 aqueous-carbonic fluids released during metamorphic reactions in middle to lower crust. Increases in
83 disequilibrium between fluids and host rock induce destabilization of gold-carrying complexes such as $\text{Au}(\text{HS})_2$
84 and AuHS (Tomkins, 2013). Possible sources of fluids for orogenic gold deposits are: (1) metamorphic rocks
85 and fluids generated with increasing metamorphism and (2) felsic intermediate magmas and associated fluids.
86 The first source is very consistent with geological, geochronological and geochemical data (Goldfarb and
87 Groves, 2015), while the second source remains inconsistent as no universal temporal link has been described to
88 date.

89

90 The Baoulé-Mossi domain (Abouchami and Boher 1990; Boher et al. 1992; Taylor et al. 1992) hosts abundant
91 gold deposits (Fig. 1) within deformed volcanic and sedimentary rocks that have undergone regional greenschist
92 to locally contact amphibolite facies metamorphism (Béziat et al. 2000, 2008; Castaing et al. 2003; Ganne et al.
93 2011).

94

95 Combined structural and Re-Os and U-Pb geochronology performed respectively on hydrothermal pyrite and
96 arsenopyrite, and hydrothermal accessory minerals such as monazite or rutile (Pigois et al., 2003; Tunks et al.,
97 2004; McFarlane, 2011; White et al., 2014), that have been considered petrographically as gold proxy (Le
98 Mignot 2016a; Le Mignot et al. 2016b; Markwitz et al., 2015) highlight two groups of orogenic gold deposits.
99 An Early-orogenic gold group formed during the Eoeburnean orogeny, i.e., between 2190 and 2125 Ma
100 (Wassa1, Kiaka1) (Perrouy et al. 2015; Le Mignot et al., 2016) while a second late-orogenic gold group hosted
101 by brittle structures, formed during late Eburnean deformation, between 2120 and 2000 Ma (Obuasi, Damang,
102 Nassara, Wassa2, Kalana, Loulo, Poura, etc). These lode gold events seem to be widespread through the West
103 African Craton (See fig. 2 in Markwitz et al., 2016; and references therein, Le Mignot et al. 2016b).

104

105 The Kiaka gold deposit is located at 140 km southeast of the capital Ouagadougou. Owned by B2Gold Corp.
106 (Volta Resources formally), the deposit has measured and indicated resources of 124 Mt at 1.09 g/t Au (3.9
107 Moz) and inferred resources of 27 Mt at 0.93 g/t Au (0.8 Moz; B2Gold Corp., January 2013). In March 2014,
108 B2Gold Corp. submitted a permitting study to the Ministry of Mines in Burkina Faso together with a mining
109 licence application.

110

111 This paper will present the geological features of the Kiaka gold deposit, one of the largest undeveloped gold
112 resources in Burkina Faso, which expresses a multistage gold mineralization. The Kiaka gold deposit is hosted
113 by metamorphosed sedimentary rocks, from greenschist to amphibolite facies that are affected by syn- to late-
114 orogenic magmatism. The relative timing of gold mineralization relative to metamorphic and magmatic events is
115 unclear. The geological features of the Kiaka deposit will be described, combining structural, petrographic,
116 mineralogical, thermobarometric and geochronological studies (U-Pb on zircon and Re-Os on pyrrhotite). The
117 timing of the gold mineralization and magmatic events will be placed within the metamorphic evolution of the
118 considered crustal segment (Ganne et al., 2011). Key geological features will be discussed for exploration
119 implication in the Baoulé-Mossi domain, a juvenile Paleoproterozoic crust that hosts major gold districts.

120

121

FIGURE 1

122

123 Regional geological framework

124

125 The West African Craton (WAC) consists of an Archean nucleus (Kénéma Man domain) that is surrounded by
126 2.25 to 2 Ga Paleoproterozoic greenstone belts of the Baoulé-Mossi domain (Feybesse and Milesi 1994;
127 Feybesse et al. 2006; Fig. 1). The Baoulé-Mossi domain comprises Birimian greenstone belts (volcanic and
128 volcano-sedimentary rocks) intruded by Tonalite-Trondhjemite-Granodiorite (TTG) suites and granitoids (Leube
129 et al. 1990; Doumbia et al. 1998; Gasquet et al. 2003; Dioh et al. 2005, Davis et al. 2015). The volcanic rocks
130 vary in composition from basalt with tholeiitic and/or calc-alkaline affinities to rhyolite. Basalts are interpreted
131 as oceanic crust (Leube et al. 1990; Ama Salah et al. 1996; Béziat et al. 2000; Baratoux et al. 2011) or oceanic
132 plateau basalts (Abouchami and Boher 1990; Boher et al. 1992; Vidal et al. 1996; Doumbia et al. 1998; Lompo
133 2009). Rhyolites are associated with juvenile calc-alkaline volcanic island arc-style rocks (Baratoux et al. 2011
134 and references therein). Tholeiitic volcanic rocks are dated at 2.17 Ga (Taylor et al. 1992; Simeon et al. 1992;
135 Hirdes and Davis 1998) and the TTG intrusions vary in age from ca. 2.25 to 2.10 Ga, representing a major
136 period of crustal growth (Hirdes et al. 1996; Doumbia et al. 1998; Lütke et al. 1998, 1999; Oberthür et al. 1998;
137 Castaing et al. 2003; Gasquet et al. 2003; Feybesse et al. 2006; Agyei Duodu et al. 2009; Siegfried et al. 2009;
138 Thomas et al. 2009; Eglinger et al. 2015). TTG magmatism was accompanied by the deposition of the Birimian
139 volcanic and sedimentary rocks (Baratoux et al., 2011). Until ca. 2.07 Ga, potassic and peraluminous granites are
140 contemporaneous with late transcurrent shearing (Hirdes et al. 1992; Davis et al., 1994; Doumbia et al. 1998;
141 Egal et al. 2002; Castaing et al. 2003; Vegas et al. 2007). Intrusive rocks have been divided into three groups
142 based on petrography, geochemistry and radiometric ages (Baratoux et al. 2011) and on airborne magnetic and
143 radiometric signatures (Metelka et al. 2011). The first magmatic episode (ME1) is characterized by calc-alkaline
144 biotite and amphibole-bearing TTG suites dated from ca. 2.16 to 2.12 Ga. The second episode (ME2) is
145 represented by calc-alkaline K-feldspar and biotite-bearing granodiorite-granite intrusions dated from ca. 2.12 to
146 2.09 Ga. The third episode (ME3) is dominated by potassic feldspar-bearing granites that are associated with late
147 orogenic stages at ca. 2.11 and 2.07 Ga. At a regional scale, multiple tectonic phases related to Eo- or -Eburnean
148 orogeny are recognized (Baratoux et al. 2011; Perrouy et al., 2012; Block et al., 2015). The D₁ deformation is
149 defined as E-W to WNW compression illustrated by isoclinal folds and local shear zones. The D₂ event is

150 defined by regional, sinistral NS trending or dextral E-NE-trending anastomosing shear zones (Baratoux et al.,
151 2011). The late-D₂ to D₃ phase is illustrated by the development of N- to NE-trending transcurrent shearing (D₂-
152 related shear zones). Following the main period of tectonic amalgamation of the various volcano-sedimentary
153 belts between ca. 2.20 and 2.15 Ga (Feybesse et al. 2006), the Baoulé-Mossi Paleoproterozoic crust was
154 deformed during the Eburnean orogeny from ca. 2.15 to 2.00 Ga (Bonhomme 1962; Feybesse et al., 2006;
155 Baratoux et al., 2011). The latter is divided in two phases: the ca. 2.250-2.150 Tangean event (Tshibubudze et al.
156 2009; Hein, 2010) or Eoeburnean (Perrouy et al. 2012), and the ca. 2.15 to 1.98 Ga Eburnean II phase (Baratoux
157 et al. 2011).

158

159 The Birimian formations are unconformably overlain by Tarkwaian, syn- to late-orogenic sedimentary sequences
160 (conglomerate and quartzite) with a maximum age varying between ca. 2.17 and 2.12 Ga (Davis et al. 1994;
161 Bossière et al. 1996; Perrouy et al. 2012, Davis et al. 2015).

162

163 The southeastern part of Burkina Faso (the Manga-Fada N’Gourma area) is characterized by a volcano-
164 sedimentary sequence and plutonic rocks, which are bounded or crosscut by high-strain shear zones (i.e. Fada
165 N’Gourma belt described by Naba et al. 2003 and Ganne et al. 2011, Fig. 2). The area is cut by the Markoye
166 shear zone (MSZ), a major N-S oriented crustal-scale structure of 450 km formed during D₁ and reactivated
167 during D₂ (Tshibubudze et al., 2009 and Tshibubudze and Hein, 2013; Fig. 2) and that crosscuts several distinct
168 volcano-sedimentary belts. This structure has recorded multiple reactivation events as distinguished by
169 Tshibubudze et al. (2009) in its northern part (North Burkina Faso). Several orogenic gold deposits are
170 associated with the MSZ within the Aribinda-Essakhane (Essakhane; Tshibubudze et al., 2015), Bouroum-
171 Yalago (Gangaol, Taparko, Béziat et al., 2008) and Manga-Fada-N’Gourma (this study) greenstone belt (Fig. 1).
172 The Kiaka gold deposit is located at the intersection between the MSZ and several smaller D₂ NE-SW trending
173 shear zones (Fig. 2). These shear zones are roughly parallel to a series of metamorphosed volcano-sedimentary
174 belts bounded by plutonic belts (Hottin and Ouédraogo 1976, 1992; Castaing et al. 2003; Naba et al. 2003;
175 Vegas et al. 2007). The Manga-Fada N’Gourma greenstone belt predominantly consists of metamorphosed
176 pelites, greywackes and volcanic rocks, including basaltic to andesitic coherent lava flows and volcanoclastic
177 rocks (Hottin and Ouédraogo 1976; Castaing et al. 2003).

178

FIGURE 2

179

180 **Materials and methods**

181

182 *Structural data*

183

184 Structural analysis was done on oriented drill core (Fig. 3) and on rare outcrops of deformed quartz-biotite
185 metagreywacke and aluminosilicate-bearing metapelites (Figs. 3 and 8). DK_x will be used to describe the
186 different deformation events described on drill cores and outcrops from the Kiaka deposit and SK_x , LK_x and FK_x
187 for foliation, lineation and folding, respectively.

188

189 *Geochemical analyses of whole rocks and minerals*

190

191 Major and trace elements (Table 1) were determined by ICP-AES and ICP-MS at the Service d'Analyse des
192 Roches et des Minéraux, Nancy (SARM, CRPG-CNRS, France) on four whole-rock samples from the volcano-
193 sedimentary (KDH291-56.2, KDH348-44.5-54.8, KDH75-64.9) and magmatic units (KDH337-44.1). Sample
194 preparation, analytical conditions, uncertainty and limits of detection are detailed in Carignan et al. (2001) and in
195 <http://helium.crpq.cnrs-nancy.fr/SARM/pages/roches.html>. For all elements, error are < 0,01% and uncertainty
196 are < 5%. Geochemical reference materials are Basalt BR, Diorite DR-N, Serpentinite UB-N, Anorthosite AN-
197 G and Granite GH (Carignan et al., 2001). Data are presented in Table 1.

198

199 *Microprobe analyses of minerals*

200

201 SEM (Hitachi S-4800 and JEOL J7600F) and microprobe analyses (Table, 2, 3, 4 and 5) by electron microprobe
202 CAMECA SX100 were performed at GeoRessources (Nancy, France). For analyses and quantitative mapping,
203 an accelerating voltage of 20 kV, beam current of 12 nA and peak counting time 10 to 20 s were used. Whole
204 rock lithogeochemical data and in situ silicates and sulfides data are presented in Tables 1 to 7. For the Table 5,
205 mineral chemical analyses within rocks were carried out at the GET at Université Toulouse III, France, using a
206 Cameca SXFIVE electron microprobe analyser. Operating conditions were 15 kV, 20 nA, 1–5 μm beam size and
207 counting time of 10 s/per element. CO_2 was neglected because no carbonates were observed in the meta-
208 sedimentary rocks analysed.

209

210 *Geothermobarometry*

211

212 Phase diagram has been used to constraint P-T conditions of the calc-silicate schists which have recorded the
213 conditions at the peak of metamorphism. These diagrams have been computed using Perple_X 6.6.8 (Connolly,
214 2005, 2009) and the updated 2002 version of the internally consistent thermodynamic database of Holland and
215 Powell (1998). For solid solutions, we used the internally consistent thermodynamic dataset termed
216 solution_model.dat (December 10, 2014; available at www.perplex.ethz.ch/).

217

218 *ICP-MS and N-TIMS Re-Os dating*

219

220 Re-Os dating on sulfides (Stein et al. 2000; Brenan et al. 2000; Reisberg and Miesel 2002, Selby et al., 2002;
221 Selby and Creaser 2004; Mathur et al. 2005; Cardon et al. 2008; Lü et al. 2011, André-Mayer et al. 2014) is a
222 useful tool for dating ore deposits. Sulfide powders, added with an appropriate quantity of a mixed ^{185}Re - ^{190}Os
223 spike and 0.1 mL of hydrogen peroxide, were dissolved in reverse aquia regia (2 mL HCl, 5 mL HNO_3) using a
224 high pressure asher (HPA-S Anton Paar). Sample digestions were carried out for 3 hours at 300°C, under 130
225 bars of confining pressure. After sample digestion, Os was separated by liquid-liquid extraction into liquid
226 bromine (Birck et al. 1997); Re was extracted from the residual solution by anion exchange using
227 chromatographic columns (AG1 X8 resin). Os was then purified by micro-distillation (Birck et al., 1997). Re
228 measurements were made using an inductively coupled plasma mass spectrometer (ICP-MS) (Neptune, in
229 CRPG, Nancy). Instrumental mass fractionation was regularly monitored during measurements using a 0.3 ppb
230 Re standard. Os was analyzed by negative thermal ionization mass spectrometry (N-TIMS; Creaser et al. 1991;
231 Völkening et al. 1991) using a Finnigan MAT 262 instrument, CRPG). Instrumental mass fractionation was
232 corrected iteratively off-line by assuming that the true $^{192}\text{Os}/^{188}\text{Os}$ ratio of the sample lay on a mixing line
233 between the natural value (3.08271) (Nier, 1937) and the measured spike value (5.00736) (Le Mignot, 2014).
234 Corrections for isobaric interferences of isotopically heavy oxides were done using the oxygen isotopic
235 composition of Nier, (1950) ($^{17}\text{O}/^{16}\text{O} = 0.0003708$ and $^{18}\text{O}/^{16}\text{O} = 0.002045$).

236 Total Os blanks linked to chemical preparation and mass spectrometric measurements range from 0.04 to 0.16
237 pg (3 analyses). The ^{187}Os contents of these blanks are comprised between 0.01 and 0.08 pg and are considered
238 as insignificant when compared to the quantities of radiogenic Os in the samples. Re blank values are higher,

239 ranging between 3.9 and 8.3 pg. They nevertheless always represent less than 0.4% of the quantities of the Re
240 present in the samples. Uncertainties related to the blank characterization are included in the total uncertainties.
241 During the period of analysis, the $^{187}\text{Os}/^{188}\text{Os}$ ratio of our in-house standard was 0.1739 ± 0.0005 (2σ , $n=52$),
242 which agrees with the value obtained for this standard over the past 8 years (0.1737 ± 0.0008 , $n=315$). Eight
243 replicates of the Henderson molybdenite standard yielded an average age of 27.75 ± 0.15 Ma (2σ -m; $n=8$),
244 slightly older than the recommended value (27.656 ± 0.022) of Markey et al. (2007).

245

246 *LA-ICP-MS U-Pb zircon dating*

247

248 Normal transmitted and reflected light microscopy, as well as cathodoluminescence imaging were used to
249 determine the internal structures of zircon prior to analysis. Analyses by Laser Ablation Inductively Coupled
250 Plasma Mass Spectrometry (LA-ICP-MS) were performed in the Geosciences Rennes laboratory, using a
251 quadripole ICP-MS Agilent 7700x coupled with a 193 nm Excimer laser system ESI (NWR193UC). More
252 details on the analytical procedure can be found in Ballouard et al. (2015). Single analyses consisted of ~20 s of
253 background integration with the laser off, followed by ~60-s integration with the laser firing and then a ~10-s
254 delay for wash out. Zircon grains were ablated using a laser repetition rate of 4 Hz, laser energy of $8\text{J}/\text{cm}^2$ and a
255 beam diameter of $30\ \mu\text{m}$ (carrier gas is He (0.75 l/min), combined with Ar (0.8ml/mn) and N₂ (3 ml/mn) using
256 in-house smoothing device). Raw data were corrected for Pb/U and Pb/Th laser-induced elemental fractionation
257 and for instrumental mass discrimination by standard bracketing with repeated measurements of the zircon
258 standard GJ-1 (Jackson et al. 2004). Together with the samples, the zircon standard 91500 (ca 1065 Ma;
259 Wiedenbeck et al. 1995) was measured as an unknown to monitor the precision and accuracy of the analyses and
260 yield a concordia age of 1068 ± 8 Ma (MSWD=1.3; N=4). Data were reduced using GLITTER (Van
261 Achterbergh et al., 2001). Analytical uncertainties are listed at 1σ (Table 8) and age determinations were
262 processed using Isoplot/Ex (Ludwig 2000). Reported data are not corrected for common Pb, however, only
263 pristine zircon domains devoid of inclusions were targeted for U-Pb geochronology.

264

265 **Local geology and deposit geometry**

266

267 *Local geology*

268

269 The geology of the Kiaka property is characterized by the structurally imbricated metamorphosed mafic rocks,
270 conglomerate, quartz-biotite or lithic metagreywacke, aluminosilicate-bearing metapelites, garnet-
271 orthopyroxene-bearing schist, and quartz-muscovite schist (Fig. 3). Garnet-orthopyroxene-bearing schists are
272 located in the southern part of the deposit, while the lithic greywackes are located in the northern part. These
273 units are usually 200-400m wide, elongated slices striking N035, commonly subparallel to D₂-related shear
274 zones. All units dip to the northwest at 80 to 85°. Thickness of the lithic greywacke varies from 50 to 100
275 meters. The garnet-orthopyroxene-bearing schist is mainly located in the footwall of the D₂-related shear zone
276 (Fig. 4). A diorite plug (5 to 30 m thick) is located in the north and is structurally controlled by D₂-related shear
277 zones.

278

FIGURE 3

279

FIGURE 4

280

281 The host rocks at the Kiaka deposit are predominantly metasedimentary (Fig. 5a, b and c) and metavolcanic
282 rocks (Fig. 5e). These include quartz-muscovite schists (Fig 5a) and garnet-orthopyroxene-bearing schist and a
283 dioritic plug (Fig. 5d) intrudes the quartz-biotite and quartz-muscovite schist in the north part of the ore body
284 (Fig. 4a). This contains clasts of amphibolite schists.

285

286 *Metasedimentary rocks*

287

288 Aluminosilicate-bearing metapelites (KDH348 – 44.5; Fig. 5c) are located in the south footwall of a DK₂-related
289 shear zone that hosts the main mineralized envelope (Fig. 3). Samples are characterized by a granoblastic to
290 nematoblastic texture (metamorphic texture in which prismatic minerals such as sillimanite or amphiboles are
291 oriented to produce a linear fabric) underscored by a shape-preferred orientation of fibrolite (15-25%) and
292 prismatic sillimanite (5-10%), the latter defining the LK₂ mineral lineation (Fig. 8b). Fine grains of quartz (50-
293 75%) dynamically recrystallized, characterizing a foliation parallel to the sillimanite orientation, are dominant in
294 the matrix. Some rounded kyanite poikiloblasts are also present, wrapped into the SK₂ schistosity. Kyanite
295 crystals replace muscovite (Ms₁; Fig. 6b). Some euhedral biotite crystals are present and locally chloritized. Fine

296 euhedral grains (20 to 50 μm) of tourmaline (Tur_1) are also observed in the recrystallized quartz-rich matrix.
 297 Lithic greywacke is characterized by feldspar or quartz porphyroclasts (100 μm to 0.1mm; 5-75%), biotite (10-
 298 25%), chlorite, and rare pyrrhotite.

299

300 *Garnet-orthopyroxene-bearing schist*

301 This schist unit (KDH300-470; Fig. 6c) comprises garnet (15-20%), orthopyroxene (10-15%), amphibole (50-
 302 55%), biotite (4-5%), plagioclase (10-15%; An_{21}), and chlorite (5-10%). Biotite and amphibole define a
 303 nematoblastic texture. Poikiloblastic garnets ($X_{\text{Alm}}:0.72$) often contain quartz, biotite, amphibole and sulfide
 304 inclusions (<50 μm). Orthopyroxene grains (Ferrosilite) are found in equigranular domains in association with
 305 amphibole (ferro-hornblende), quartz and phlogopite (Bt_1). Chlorite (Chl_1) is associated with amphibole and
 306 biotite (Bt_1) crystals.

307

308 *Diorite*

309 Samples KDH337-44.1 and -69.6 (Fig. 6d) are from the 6100 section, 300 m northeast of the 5800 cross-section
 310 (Fig. 4a). Located in the north part of the deposit area, no clear relationships with the stage 1 was observed but
 311 sericite, calcite and clinozoisite, pyrrhotite and chalcopyrite are locally present in the intrusion as alteration
 312 assemblage related to strained domains. The assemblage is made up of plagioclase (25-30%; An_{27}), amphibole
 313 (25-30%), chlorite, biotite (20-25%), and quartz (15-20%), with minor amounts of sulfide (1-2 % of pyrrhotite
 314 sometimes associated with rare chalcopyrite) and zircon. Amphibole porphyroblasts (200-500 μm) are rimmed by
 315 biotite forming corona textures (Fig. 6d). Amphiboles have Mg-hornblende to actinolite compositions with X_{Mg}
 316 ranging from 0.55 to 0.95 and Ca (apfu) ranging from 1.66 to 2.00 (Table 5).

317

318 **FIGURE 5**

319 **FIGURE 6**

320

321

322 *Geometry of the deposit*

323

324 Four mineralized envelopes at the Kiaka deposit are defined based on drill core data (Fig. 3). Each subparallel
 325 envelope is hosted elongated ore bodies mostly hosted by the quartz-biotite metagreywacke underlying the lithic

326 metagreywackes (Figs. 3 and 4b). Lithological contacts are mineralized in 6100 and 5400 sections. In section
327 5800, the main ore zone is developed in an axial plane of a FK₂ isoclinal fold illustrated by the geometry of the
328 lithic greywacke and also at the contact with D₂ related shear zones that probably juxtaposed this unit with the
329 garnet-orthopyroxene-bearing schist.

330

331

332 **Geochemistry**

333

334 Quartz-muscovite schists (KDH75-64.9) and aluminosilicate-bearing metapelites (KDH348-44.5) have high
335 SiO₂ (78.01 wt.% and 71.66 wt.%) and Al₂O₃ (13.55 wt.% and 15.14 wt.%). Major element analyses of the
336 meta-igneous sample KDH337 show intermediate SiO₂ (57.32 wt.%) and high Al₂O₃ (16.59 wt.%) and CaO
337 (6.57 wt.%) concentrations combined with a total alkali (Na₂O + K₂O = 5.72 wt.%) content and a K₂O/ Na₂O
338 ratio of 0.53 indicating an affinity with the sodic series (Table 1). On the SiO₂ vs. Na₂O + K₂O binary diagram of
339 Cox et al. (1979), this intrusion plots in the field of diorite (Fig. 7a). The Kiaka diorite has high Sr and Ba
340 concentrations, of 748 and 665 ppm, respectively (Table 1). This rock is characterized by strong depletions in
341 Nb, Ta and Ti and a positive Sr anomaly and displays no Eu anomaly, as shown by the primitive mantle-
342 normalized spidergram (Fig. 7b). The Sr/Y ratio is high (~47) compared to the Tenkodogo granitoid (~27; Naba
343 et al., 2003; See Table 1 for details), located 50 km east of the Kiaka gold deposit. The rare earth elements
344 (REE) are fractionated and characterized by low HREE abundances (Yb = 1.48 ppm) and a high (La/Yb)_N ratio
345 (~13; N indicates chondrite normalization after Sun and McDonough, 1995). However, fractionation among the
346 HREE is moderate, as is indicated by the Y/Yb ratio of ~11 and the flat HREE patterns (Fig. 7c). Diorites from
347 the Morila Au deposit (McFarlane et al., 2011), granitoids from Tenkodogo (samples T15 and DD17; Naba et
348 al., 2003) and Fada'N'Gourma area (sample FC97; Vegas et al, 2007) express similar major and trace elements
349 composition.

350

351

TABLE 1

352

FIGURE 7

353

354 **Structural data**

355

356 *DK₁ event: Early penetrative foliation*

357

358 The first event DK₁ is evidenced by the presence of relic FK₁ folds (Fig. 8a) evidenced by a wide range of fold
359 axis orientations with a moderate plunge (45° to 60°) that diverged from the isoclinal folds with axial planes
360 parallel to the SK₂ cleavage (Fig. 8d). The aluminosilicate-bearing metapelites are affected by such FK₁ folds as
361 illustrated by FK₁/FK₂ interference patterns (Fig. 8e) whereas mafic rocks are unaffected by such early
362 deformation (Fig. 8c).

363

364 *DK₂ event: Metamorphic foliation, shear-related folds and late-DK₂ shear zones*

365

366 Stretching and mineral lineations LK₂ (Fig. 8b) oriented N352 to N070 with moderate plunges from 52° to 64°
367 are associated with the axial planar SK₂ cleavage/foliation. Prismatic sillimanite commonly defines this mineral
368 lineation. Moderate plunge of ore shoots illustrates effects of oblique shearing along the D₂-related shear zones
369 and/or effects of shallow plunging of the FK₂ fold axis on ore distribution (Fig. 4d). Shear-related asymmetric
370 folds (Fig. 8d) and shear zones oriented 050NE, plunge steeply to the North (Fig. 4b). Sigma-type
371 porphyroclasts and C-S shear bands indicate a sinistral movement (Fig. 8d). Section view illustrates the reverse
372 component of this structural event. These shear zones are spatially associated with the ore zones hosted by the
373 volcano-sedimentary units of the Manga-Fada-N'Gourma area. Ore shoots are roughly collinear with the LK₂
374 lineation (Figs. 4d) but sometimes appear as following stratigraphic folded contacts or DK₂-related shear zones
375 (Fig. 4b). FK₂ folds limbs are totally transposed in the SK₂ regional foliation and related shear bands. Late-D₂
376 ME₂₊₃ plutons (Ouargaye and Kaouré) are affected by regional D₂-shear zone reactivations (Fig. 2). The diorite
377 intrusion (dated in this study) located in the NE of the deposit are locally affected by shearing, illustrated by the
378 alignment of biotite sheets and actinolite grains.

379

380 *DK₃₋₄ events: Late fracture-controlled veining associated with reactivation along DK₂ shear zones*

381

382 Based on their orientations and crosscutting relationships (Fig. 11c and e), a distinction is made between DK₃
383 (N010°) and DK₄ (N100°) faults. DK₄ quartz veins with slivers of metamorphosed and hydrothermally altered
384 metagreywackes, quartz-carbonate-phlogopite or quartz-carbonate extensional veins form a fractured-controlled
385 stockwork locally reworked and reoriented along the SK₂ fabric, preferentially developed at the contact between

386 the metasedimentary sequence and metamorphosed mafic rocks (See Hydrothermal alteration for details).
387 Orientations and dips of DK_{3,4} veins have NE to SW-trending a wide range of dips (15 to 85°) with NE to SW-
388 trending orientations.

389 **FIGURE 8**

390 **FIGURE 9**

391

392 **Metamorphism**

393

394 We investigated the metamorphic history using a combination of conventional geothermobarometry (chlorite,
395 amphibole and arsenopyrite) and metamorphic modelling.

396

397 *Conventional geothermobarometry*

398

399 Chlorite temperatures (Table 2) were calculated using the thermodynamic modeling program of Lanari et al.
400 (2014). Chlorite inclusions (Chl₁; Fig. 11e) in tourmaline porphyroblasts from the metabasic sample KDH29-
401 56.2 yielded the lowest temperatures ranging from 269 to 306 °C, corresponding to a mean temperature of 285 ±
402 50°C (n=4; Table 2). A 2nd generation of chlorite is associated destabilization of biotite porphyroblasts within
403 metabasic rock. This local chloritization stage (Chl₂; Fig. 11) observed in the matrix occurred at temperatures
404 ranging from 371 to 413 °C, corresponding to a mean temperature of 383 ± 50°C (n=7; Table 2).

405

406 **TABLE 2**

407

408 Major element compositions of calcic-amphibole from the diorites collected in drillhole KDH337 were analyzed
409 in order to estimate pressure of emplacement (Table 3). From the cores of porphyroblasts, amphiboles associated
410 with biotite (Fig. 10f) are mainly actinolite, but Mg-hornblende is also present (Table 3). We interpret the latter
411 as relicts of magmatic amphibole that was formed during prograde metamorphism and preserved from
412 retrogression and potential coeval hydrothermal alteration. Four different geobarometers (Hammarstrom and
413 Zen, 1986; Hollister et al., 1987; Johnson and Rutherford, 1989 and Schmidt, 1992) were applied to each of the
414 three Mg-hornblende crystals tested. Pressure estimates (Table 3) ranged from 0.92 to 5.65 kbars indicating
415 variable degrees of re-equilibration during retrogression or hydrothermal circulation.

416

417

TABLE 3

418

419 *Metamorphic modeling*

420

421 A pseudosection approach appears appropriate for assessing changing mineral paragenesis in rock types of
 422 homogeneous composition. Our pelitic samples (KDH300-470), collected in the interference zones of the Kiaka
 423 area, with a variable D₂ imprint, are characterized by a homogeneous distribution of zoned minerals, such as
 424 garnet and orthopyroxene that are unlikely to have modified the bulk rock composition during their growth. The
 425 P-T pseudosection were calculated for the Na₂O–CaO–K₂O–FeO–MgO–MnO–Al₂O₃–TiO₂–SiO₂–H₂O system,
 426 using bulk rock compositions obtained by XRF analysis and for subsolidus H₂O saturations conditions. The
 427 observed mineral assemblage, i.e. garnet-biotite-chlorite-plagioclase-orthopyroxene and orthoamphibole with the
 428 presence of ilmenite, ± K-feldspar and ± quartz is bivariant and stable over a narrow *P–T* range at 7.5 – 4 kbar and
 429 550 - 400 °C. Perple_X modeling using the compositions of biotite observed as inclusions within the rim of
 430 garnets (Table 4) allows the refinement of the inferred peak of metamorphism at P=7.5 kbar and T=550 °C. At
 431 this calculated peak, mineral phases are orthopyroxene (6.00 vol%), biotite (3.10 vol%), chlorite (6.71 vol%),
 432 plagioclase (65.32 vol%), K-feldspar (6.01 vol%), garnet (2.67 vol%), ilmenite (0.84 vol%), quartz (0.09 vol%)
 433 and orthoamphibole (9.25 vol%). These mineral proportions are in good agreement with thin section observation
 434 (Fig. 6c). Conditions are regarded as coeval with the DK₂ deformation and diorite emplacement. The Kiaka
 435 sedimentary host rocks underwent the M2a prograde near-isobaric heating at 450-650 and 6-8kbar described by
 436 Ganne et al., 2014 in metasediments located in high-T aureoles of granitoids plutons recorded.

437

438

TABLE 4

439

Mineralization

441

442 Two stages of gold mineralization are identified based on crosscutting relationships, hydrothermal assemblages
 443 and ore mineralogy: an early sulfide-rich disseminated stage 1 and a sulfide-poor stage 2. Stage 1 represents at
 444 least 80% of the volume of the ore bodies and is located in the quartz-biotite and lithic metagreywackes
 445 extending 10 to 150 m from DK₂ high-strain zones. Stage 2 is associated with strongly altered stratigraphic

446 contact affected by D₂-related shear zones. Temporal relationships between host rocks, gangue, and ore minerals
447 are summarized in Figure 10. Figures 11 and 12, respectively, illustrate mineralization styles, ore mineralogy,
448 and textures.

449 **FIGURE 10**

450 *Ore styles and textures*

451

452 A wide range of mineralization styles is present at Kiaka including i) a stockwerk of semi-massive pyrrhotite,
453 pyrite and chalcopyrite in association with replacement zones of biotite-clinozoisite (70-80% of ore), ii)
454 hydrothermal breccia composed of hydrothermally altered fragments of pelites, the quartz-rich matrix locally
455 containing diopside and actinolite (10-15% of ore; Fig. 11b), and iii) a network of quartz carbonate veinlets
456 associated with a pervasive alteration assemblage composed of clinozoisite and carbonate (5-10%) and iv)
457 quartz-carbonate-phlogopite veins (rare DK₄). The latter three styles commonly overprint the sulfide dominant
458 ore stage (Fig. 11b, c, d and e).

459

460

FIGURE 11

461

462 *Ore mineralogy*

463

464 Pyrrhotite (50 μm to 1 mm) accounts for 60-80% of ore phases characterizing the mineralization in stage 1.465 Pyrrhotite is commonly associated with 10 to 20% of pyrite (200-300 μm), 5 to 10% of chalcopyrite (20-50466 μm), 5-10% of pyrite (50 to 200 μm), 5-10% of arsenopyrite (100 to 500 μm) and rare löllingite inclusions467 within pyrrhotite or arsenopyrite (<50 μm). Pyrite forms overgrowths or composite aggregates with

468 pyrrhotite and chalcopyrite. Pyrrhotite grains are commonly inclusion-rich (chalcopyrite, quartz and

469 hematite) and fracture-filling chalcopyrite. These sulfides comprise recrystallized aggregates transposed

470 within the SK_2 foliation (Fig. 12a) and locally affected by shearing along DK_2 shear bands (Fig. 11a and

471 Fig. 13a). These characterize the large mineralized envelope of high-grade ore. Some sulfide phases are

472 locally remobilized within necks of elongated microlithons of quartz-rich matrix (Fig 12a). Arsenopyrite is

473 is partially to totally replace by pyrrhotite aggregates (Fig. 12c). Inclusions of löllingite within pyrrhotite

474 crystals are present in strongly sericitized greywacke (Fig 12c).

475

476 The stage 2 contains less abundant sulfides (< 2-3 %) but Bi-Te-rich phases (5-10 μm), electrum (10 to 20477 μm), and native gold (2 to 20 μm) are associated with chalcopyrite, pyrrhotite and arsenopyrite (Fig. 12d, e

478 and f). Electrum is found in i) fractures within pyrrhotite, arsenopyrite (Fig. 12e), chalcopyrite and

479 clinozoisite, ii) in chlorite sheets (Fig 12f). Finally, fractures in arsenopyrite associated with electrum in

480 fractures (Fig. 12e).

481

482

FIGURE 12

483

484 Co content of arsenopyrite (Table 5 and Fig. 12e) are highly variable between arsenopyrite from sericitized

485 greywacke ranging from 0.04 to 0.13 wt.% (mean of 0.08 wt.% Co; n=6) or associated with Chl_2 in chloritized

486 greywacke ranging from 4.52 to 5.41 wt.% (mean of 4.96 wt.% Co; n=2). Arsenic content of arsenopyrites

487 (Table 5) in contact with pyrrhotite and löllingite in quartz-biotite metagreywacke ranges from 35.44 to 36.45 (%)

488 atm), yielding a temperature of 360 to 475°C based on geothermometer of Sharp et al. (1985).

489

TABLE 5

490

491 **Hydrothermal alteration**

492

493 Various styles of hydrothermal alteration are observed in association with the mineralized envelope (Fig. 11 and
 494 13). We summarize the hydrothermal alteration type into six types including biotitization, tourmalinization, calc-
 495 silicate alteration, sericitization and chloritization-carbonatization.

496

497 *Biotitization*

498

499 The most typical alteration type is biotitization which represented 70-80% of the alteration assemblage within
 500 mineralized envelope (Fig. 13a). Biotite sheets (Bt_2) defined elongated replacements zones, associated with
 501 subautomorph clinozoisite crystals (10-15%) developed on primary feldspars (10 to 40% of the whole rock) that
 502 contrasts with smaller euhedral biotite crystals (Bt_1). Three biotite generations (Table 6) are defined: 1) euhedral
 503 phlogopite grains (Bt_1) characterized by a X_{Mg} from 0.543 to 0.585 and TiO_2 content from 1.33 to 1.68 wt.%
 504 (Fig. 13b and d); 2) xenomorphic sheets of phlogopite in the matrix (Bt_2 ; Fig. 13a) with low X_{Mg} (0.37) and high
 505 TiO_2 (2.40 wt.%); and 3) phlogopite (Bt_3) within quartz-carbonate-gold veins, with X_{Mg} ranging from 0.558 to
 506 0.583 and TiO_2 content ranging from 1.28 to 1.51 wt.% (Fig. 12d). Bt_2 is paragenetically later than Bt_1 (Bt_2 is
 507 associated with tourmaline and sulfides), is partially chloritized, and associated with sulfides and clinozoisite.
 508 Bt_2 phlogopite grains define a weakly penetrative schistosity. This alteration type is commonly overprinted by a
 509 chlorite-carbonate alteration assemblage.

510

TABLE 6

511

512 *Tourmalinisation*

513

514 More rarely (5-10% of alteration assemblage), tourmalinisation is developed in aluminosilicate-bearing
 515 greywacke and within strongly altered quartz-biotite or lithic greywacke. Primary tourmaline (Tur_1) are locally
 516 present (rare to 5%) in the quartz-rich matrix of aluminosilicate-bearing greywacke (Fig. 6a) as rounded grains
 517 ($<10 \mu m$). Analysed tourmaline grains (Tur_2) have composition of Mg-foitite (Table 7) and can contain sulfide
 518 inclusions (50-100 μm), quartz and apatite inclusions. Locally, a porphyroblastic texture represented by
 519 tourmaline crystals (Tur_2) ranging in size from 50 to 600 μm are developed. The matrix is dominated by biotite

520 (Bt₂), chlorite (Chl₂), clinozoisite, titanite, sulfide, carbonate and plagioclase. Tourmaline grains (Tur₂) have a
 521 various composition including dravite, to uvite to Mg-Foite composition (Table 7) with X_{Fe} ranging from 0.20
 522 to 0.72 and TiO₂ content ranging from 0.17 to 1.09 wt.%. Biotite grains are typically phlogopitic with X_{Mg}
 523 ranging from 0.59 to 0.60 and TiO₂ content ranging from 1.00 to 1.15 wt.%.

524 **TABLE 7**

525
 526 *Calc-silicate alteration*

527
 528 Calc-silicate alteration is related to hydrothermal brecciation and veining network during DK₃ hydrothermal
 529 event (Fig. 11b, c). Actinolite, clinozoisite and carbonate are located in replacement zones associated with
 530 destabilization of feldspars while diopside (20-50 μm) is located within silica flooding (Fig. 11b) or quartz veins
 531 (Fig. 11c). The increasing proportion of DK₃ calc-silicate veinlets and silicification form hydrothermal breccia
 532 with altered pelitic clasts (Fig. 11b).

533
 534 *Sericitization*

535
 536 Sericitization is developed in aluminosilicate-bearing greywacke (45 to 75% of the hydrothermal mineral
 537 assemblage) and locally within the diorite intrusion (Fig. 13f). Sericite (<10 μm; Ms₂) is developed in
 538 association with the destabilization of feldspar in the greywacke matrix spatially associated with minor
 539 amount of clinozoisite (< 5%) and disseminated tourmaline or in veinlet selvages (Fig. 13c).

540
 541 *Chloritization-Carbonatization*

542
 543 Chloritization and carbonatization are associated with vein selvages (Fig. 13d) and sometimes massive alteration
 544 bands which overprinted the biotite-tourmaline alteration assemblage (Bt₂ and Tur₂; Fig. 11d and e).
 545 Characterized by millimetric to plurimillimetric sheets of chlorite commonly developed on biotite crystals (Fig.
 546 11e and Fig 13e). These are associated with elevated gold grades ranging between 50 and 60 g/t of Au. All of the
 547 compositions measured for the chlorite (Chl₂) found in the matrix fall along the binary lines between clinocllore
 548 and corundophilite, with Si content ranging from 2.64 to 2.72 apfu and X_{Mg} ranging from 0.51 to 0.65. Chlorite

549 grains (Chl_1) in inclusion within tourmaline crystals (Tur_2) have higher Si content ranging from 2.73 to 2.94 apfu
 550 and X_{Mg} ranging from 0.63 to 0.66.

551

552

FIGURE 13

553 **Geochronology**

554

555 *U-Pb dating of the KDH337 diorite*

556

557 More than 50 zircon grains were separated for LA-ICPMS U-Pb dating of the diorite intrusion. They are
 558 characterized by subeuhedral shapes and sizes ranging from 100 to 200 μm (Fig. 14). Twenty-two grains were
 559 analyzed (Table 8). Fifteen of them ($\pm 1\%$ of discordancy; italic in Table 8) yield a concordia age of 2140.4 ± 7.2
 560 Ma (MSWD = 2; n = 15) that we interpret as the emplacement age for this diorite. If all the data are taken into
 561 account, we end up with a similar, weighted average $^{207}Pb/^{206}Pb$ age of 2140.1 ± 7.9 Ma (MSWD = 0.42, n =
 562 22).

563

564

FIGURE 14

565

TABLE 8

566

567 *Re-Os dating on pyrrhotite*

568

569 In order to provide geochronological constraints on the mineralizing events, pyrrhotite crystals were selected for
 570 Re-Os dating. However, close association between electrum, pyrrhotite and other sulfides (chalcopyrite,
 571 arsenopyrite) in zones presenting evidences of reworking and remobilization (Fig. 12a, b and c) made it difficult
 572 to obtain pure mineral separates, which may impact on the accuracy of the ages. The effect of other sulfide
 573 phases was minimized by selecting the sample KDH280-101 m, contains the least amount of chalcopyrite and
 574 pyrite (<5% of sulfides phases) compared to pyrrhotite. DK_2 -foliated pyrrhotite grains associated with low-grade
 575 gold mineralization in quartz-biotite metagreywackes were analyzed in order to constrain the age of the early
 576 gold mineralization event.

577 Results of the Re-Os dating of pyrrhotite grains are given in Table 8. The ^{187}Re contents of the analyzed
 578 pyrrhotites are around 2.3-2.4 ppb, while ^{187}Os varies from 54.4 to 57.4 ppt. In all cases, more than 99% of the

579 measured ^{187}Os is radiogenic in nature, based on the measured ^{188}Os content and assuming a common $^{187}\text{Os}/^{188}\text{Os}$
580 ratio of 0.5 ± 0.4 . As it was impossible to constrain the initial $^{187}\text{Os}/^{188}\text{Os}$ ratio directly from the data, this value
581 was chosen to include potential common Os compositions ranging from mantle to crustal values at 2 Ga. As
582 nearly all of the Os is radiogenic in nature, Re-Os ages can be calculated from individual samples. Three
583 replicates yield reproducible dates between 2168 and 2150 Ma, and provide a weighted average date of $2157 \pm$
584 24 Ma (MSWD = 2.5; n = 3). If the Os in the pyrrhotite is derived from a mantle source, the age would be close
585 to the upper limit of this range.

586

587

TABLE 9

588

589 Discussion

590

591 *Key features and implications for exploration*

592

593 This study is the first detailed description of the local geology associated with the Kiaka gold deposit. Major
594 insights are linked to four key observations, including: i) cross-cutting hydrothermal alteration with distinct
595 styles and mineral assemblages, ii) the close spatial link between D_2 -related fold hinges and/or shear zones and
596 gold distribution (Fig. 4b, c and d), iii) the lithic greywacke and/or the quartz-biotite greywacke (Fig. 5), as
597 preferential host rocks for disseminated-style of gold mineralization (Fig. 4, Fig. 11a), and iv) the mineralized
598 contacts between contrasting lithologies such as quartz-biotite metagreywackes, aluminosilicate-bearing
599 metapelites, gabbro, and orthopyroxene-garnet schist. Shear zone intersection (N-S and N-trending) and the
600 association with lithological boundaries are also potentially critical for exploration as those features are
601 ubiquitous in the Kiaka gold deposit (e.g. hinges illustrated by the lithic greywacke geometry, contact between
602 garnet-orthopyroxene-bearing schist and lithic greywacke and/or D_2 -related shear zone).

603

604 Located in the north part of the ore bodies, the Kiaka diorite shows evidence of local shearing (D_2 -related),
605 record a retrogression overprint and chlorite-carbonate alteration assemblage with minor amount of pyrrhotite
606 and chalcopyrite supporting its emplacement before D_3 or D_4 hydrothermal events. No clear relationship with the
607 stage 1 of mineralization and the diorite intrusion is observed but some small ore bodies appear to cut across or
608 developed at the contact with small dioritic dykes (Fig.4a). Our data supports close spatial and temporal

609 relationships between deformation (D₂, D₃ and D₄), gold, diorite magmatism and amphibolite facies
610 metamorphism, a feature also described in the Baoulé-Mossi domain (John et al. 1999; Debat et al. 2003; Ganne
611 et al. 2011; McFarlane et al., 2011), in the Trans Hudson orogen (Lawley et al., 2016) and the Lupa goldfield
612 (Lawley et al., 2013).

613

614 *New insights into the timing of gold mineralization*

615

616 Re-Os dating of syn-SK₂ xenomorphic pyrrhotite (possibly mixed with some chalcopyrite and arsenopyrite)
617 yields a weighted average Re-Os age of 2157 ± 24 Ma (MSWD=0.25; n=3). At microscopic scale, sulfides are
618 often stretched along the metamorphic SK₂ foliation (Fig. 11a), and sometimes remobilized in pressure shadows
619 of sillimanite-kyanite porphyroblasts (Fig. 12a). These petrographic observations suggest that pyrrhotite,
620 together with biotite, are associated with the pre- to early-SK₂ gold mineralization. Thus, this date also provides
621 a minimum age constrain on the early mineralizing event at ca. 570°C supported by the presence of pyrrhotite,
622 arsenopyrite and löllingite in equilibrium. However, Re-Os data on pyrrhotite grains have to be interpreted with
623 caution because of the low closing temperature for this mineral in association with rhenium and osmium
624 diffusion within pyrrhotite crystals (300 – 400 °C, Brenan et al. 2000). This age suggests an early lode gold
625 event during the Eburnean orogeny at ~2150 Ma as proposed in other lode gold deposit through the West
626 African Craton (Le Mignot et al., 2016b). The late gold endowment associated with DK₃ and DK₄ may be
627 related to the early or the later lode gold event described at ~2100-2040 Ma at the Wassa (Perrouy et al. 2015,
628 Parra-Avila et al. 2015, Le Mignot et al. 2016b), Damang (Pigois et al. 2003, White et al. 2014), Obuasi (Milesi
629 et al. 1992, Allibone et al. 2002, Fougrouse et al. 2016), Loulo (Lawrence et al. 2013 ; Lambert-Smith et al.,
630 2016a and b), and Nassara deposits (Ouiya et al. 2015, Le Mignot et al. 2016b). The two gold events described
631 here in Kiaka illustrate the polyphase character of the Paleoproterozoic gold mineralization (Lawrence et al.,
632 2013, Eglinger et al., 2015, Le Mignot et al., 2016b). This polyphase character has been described throughout
633 the West African Craton, but also in other Proterozoic orogenic gold districts as in the Churchill province
634 (Lawley et al., 2016); in the Ubendian belt (Lawley et al., 2013; Kazimoto et al. 2015) and in the Guyana shield
635 (Daoust et al., 2011).

636

637 The onset of the Eburnean orogeny (~2150 Ma) is a critical period where early-structures (~2160 Ma) were
638 potentially reactivated in reverse shear zones and act as major pathways for gold-bearing fluids. The Markoye

639 shear zone is an important metallotect for gold as at least two world-class gold deposits (Essakhane and Kiaka,
640 Fig. 1) are located nearby (Figure 2). Our dates (Re-Os and U-Pb) are concomitant with a long-lived D_2 regional
641 tectonic event (Fig. 16), M_2 metamorphism and magmatic activity. Interestingly, our new diorite age (2140 ± 7
642 Ma), which constrains the timing of D_2 , is slightly younger than the weighted average Re-Os pyrrhotite age at
643 (2157 ± 24 Ma), suggesting that the early disseminated gold stage may pre-date D_2 . As the Kiaka diorite is
644 locally deformed, we associate its emplacement with syn- or late- D_2 . The nearby Kaouré (2128 ± 6 Ma; Castaing
645 et al. 2003) and Ouargaye granites (2135 ± 6 Ma by U-Th-Pb on monazite; Castaing et al., 2003) are younger Z-
646 shaped intrusions controlled and/or affected by two sinistral shear zones. We therefore suggest that transcurrent
647 reactivations of D_2 -related shear zones occurred between 2140 to 2100 Ma (this study and Vegas et al. 2007) and
648 was potentially associated with D_3 and D_4 hydrothermal circulation and higher gold grades.

649

650

FIGURE 15

651

FIGURE 16

652

653 **Conclusion**

654

655 The Kiaka gold deposit has been studied using a multidisciplinary approach including field observations, core
656 logging, petrography, geothermobarometry, and geochronology. Four deformation events have been recognized
657 in the local area and at least two of them play an important role in gold distribution and concentration. The key
658 features highlighted by this study of the Kiaka gold deposit are as follows:

659

- 660 1. The host rocks are metamorphosed volcano-sedimentary rocks including quartz-biotite metagreywacke, lithic
661 metagreywacke, quartz-muscovite schist, aluminosilicate-bearing metapelites and garnet-orthopyroxene schist.
- 662 2. The deposit is located at the intersection of the D_1 N-S Markoye shear zone and the DK_2 -related NE-trending
663 shear zones. The latter strongly controlled the geometry of the volcano-sedimentary sequence illustrated by
664 structures such as FK_1 , FK_2 folds, DK_2 -related shear bands and mineral LK_2 lineations.
- 665 3. Four subparallel elongated ore bodies are hosted by the quartz-biotite metagreywackes, aluminosilicate-
666 bearing metapelites and the lithic metagreywackes and some is developed in an apparent axial plane of the DK_2
667 isoclinal folds.

668 4. Hydrothermal alteration related to gold occurs as i) pervasive alteration zones dominated by biotite and
669 clinozoizite during the DK₂ event (disseminated stage) and ii) calc-silicate monomineral or bimineral DK₃ veins
670 and veinlets (diopside, actinolite) and DK₄ pervasive muscovite, chlorite and calcite in quartz-carbonates vein
671 selvages (vein stage).

672 5. Based on crosscutting relationships, mineral assemblages and mineralization styles, two stages of gold
673 mineralization are recognized: an early disseminated stage with pyrrhotite ± pyrite, chalcopyrite (1-3 g/t Au) and
674 a late vein stage with pyrrhotite, arsenopyrite, electrum, native gold and tellurobismuthite (50-60 g/t Au) .

675 6. The emplacement of a dioritic intrusion, dated at 2140 ± 7 Ma (concordia ²⁰⁷Pb/²⁰⁶Pb age on magmatic
676 zircon), is contemporaneous with displacement along mineralized, sinistral-reverse D₂-related shear zones. The
677 early disseminated sulfide stage is dated at 2157 ± 24 Ma (Re-Os age), the first absolute age of Au
678 mineralisation in the Manga Fada N’Gourma area. This could correspond to the early lode gold event in the
679 Baoule-Mossi at ~2150 Ma.

680

681 **Acknowledgements**

682

683 We are grateful to Didier Kaboré, Michael Baddy Wanye and geologists from Volta Resources (now B2Gold
684 Corp.) for logistical aid and organization that provided us with optimal conditions for fieldwork and also for
685 authorization to publish. Discussions during field work on Burkina Faso geology with Didier Béziat, and Seta
686 Naba greatly improved the manuscript. Lenka Baratoux (IRD in Dakar) is deeply thanked for sharing her
687 understanding of the geology and metamorphic events during the Eburnean orogeny. Re-Os manipulations
688 wouldn’t have been possible without the technical support of Catherine Zimmerman and Christiane Parmentier.
689 Staff from the lithopreparation lab (Cedric Demeurie and Alexandre Flammang) and SCMEM (Service Commun
690 de Microscopies Electroniques et de Microanalyses, GeoRessources) are thanked for thin sections and imagery
691 using the electron microprobe and SEM, respectively. The senior author would like to thank Alain Cheilletz for
692 precious advice and suggestions for this study and Marie Lefebvre for biotite data acquisition. Finally, we are
693 grateful to AMIRA International and industry sponsors, including AusAid and the ARC Linkage Project
694 LP110100667, for their support on the WAXI project (P934A). This study is part of the WAXI 2 program
695 (<http://waxi2.org/>). Luc Siebenaller acknowledges the Luxemburgish Fonds National de la Recherche (FNR) for
696 the AFR post-doc grant (PDR-09-029) he benefited to conduct part of this research. Constructive and detailed

697 reviews by James Lambert-Smith and Christopher Lawley greatly improve the manuscript and help to clarify
698 many key points.

699

700 **References**

701

702 Abouchami, W., Boher, M, 1990. A Major 2.1 Ga Event of Mafic Magmatism in West Africa: An Early Stage of
703 Crustal Accretion. *J Geophys Res B Solid Earth and Planets* 95(17):605-617

704 Agyei Duodu J, Loh GK, Hirdes W, Boamah KO, Baba M, Anokwa YM, Asare C, Brakohiapa E, Mensah RB,
705 Okla R, Toloczyki M, Davis DW, Glück S (2009) Geological Map of Ghana 1:1,000,000. BGS/GGS,
706 Accra, Ghana/Hannover, Germany

707 Allibone, A., Teasdale, J., Cameron, G., Etheridge, M., Uttley P., Soboh, A., Appiah-Kubi, J., Adanu, A.,
708 Arthur, R., Mamphey, J., Odoom, B., Zuta, J., Tsikata, A., Pataye, F., Famiyeh, S., Lamb, E., 2002.
709 Timing and structural controls on gold mineralization at the Bogoso gold mine, Ghana, West Africa.
710 *Economic Geology* 97, 949-969

711 Ama, Salah, I., Liegeois, JP., Pouclet, A., 1996. Evolution d'un arc insulaire océanique birimien précoce au
712 Liptako nigérien (Sirba): géologie, géochronologie et géochimie. *Journal of African Earth Sciences* 22,
713 235-254

714 André-Mayer, AS., Ramiandrisoa, N., Vanderhaeghe, O., Reisberg, L., Rabeandrasana, S., Zimmermann, C.,
715 2014, Re-Os geochronological constraints on the Dabolava mesothermal gold occurrence, Madagascar:
716 Implications for the Ikalamavony sub-domain deposition age. *Journal of African Earth Sciences* 94,
717 119-127

718 B2Gold Corp (2013) Joint News release B2Gold Corp. agrees to acquire Volta Resources Inc.
719 (<http://b2gold.mwnewsroom.com/Files/9b/9b6b423f-7a7f-4b95-a1ba-384247c09540.pdf>)

720 Ballouard, C., Boulvais, P., Poujol, M., Gapais, D., Yamato, P., Tartèse, R., Cuney, M., 2015. Tectonic record,
721 magmatic history and hydrothermal alteration in the Hercynian Guérande leucogranite, Armorican
722 Massif, France. *Lithos* 220-223:1-22

723 Baratoux, L., Metelka, V., Naba, S., Jessell, WM., Grégoire, M, Ganne, J., 2011. Juvenile Paleoproterozoic crust
724 evolution during the Eburnean orogeny (~2.2–2.0 Ga), western Burkina Faso. *Precambrian Research*
725 191:18-45

- 726 Baratoux, L., Béziat, D., Block, S., Davis, J., Dioh, E., Fontaine, A., Ganne, J., Kennedy, K., Miller, J., Parra, L.,
727 Perrouy, S., Siebenaller, L., 2013. Thermal evolution of the Ore-bearing Birimian Provinces:
728 Unpublished Report, Module 1.4, Final Report P934A- West African Exploration Initiative-Stage 2,
729 924 p
- 730 Béziat, D., Bourges, F., Debat, P., Lompo, M., Martin, F., Tollon, F., 2000. A Palaeoproterozoic ultramafic-
731 mafic assemblage and associated volcanic rocks of the Boromo greenstone belt: fractionates originating
732 from island-arc volcanic activity in the West African craton. *Precambrian Research* 101, 25-47.
- 733 Béziat, D., Dubois, M., Debat, P., Nikiéma, S., Salvi, S., Tollon, F., 2008. Gold metallogeny in the Birimian
734 craton of Burkina Faso (West Africa). *Journal of African Earth Sciences* 50, 215-233.
- 735 Birck, J.L., Barman, M., Capmas F (1997) Re-Os isotopic measurements at the femtomole level in natural
736 samples. *Geostandards Newsletter* 20, 19-27.
- 737 Block, S., Ganne, J., Baratoux, L., Zeh, A., Parra, L.A., Jessell, M., Ailleres, L., Siebenaller, L., Mensah, E.,
738 2015. Petrological and geochronological constraints on lower crust exhumation during Paleoproterozoic
739 (Eburnean) orogeny, NW Ghana, West African craton. *Journal of Metamorphic Geology* 33, 463-494.
- 740 Boher, M., Abouchami, W., Michard, A., Albarede, F., Arndt, N.T., 1992. Crustal Growth in West Africa at 2.1
741 Ga. *Journal of Geophysical Research* 97, 345-369.
- 742 Böhlke, J.K., 1982. Orogenic (metamorphic-hosted) gold-quartz veins. US Geological Survey Open File Report
743 795, 70-76.
- 744 Bonhomme, M., 1962. Contribution à l'étude géochronologique de la plate-forme de l'Ouest africain.
745 Unpublished PhD thesis, Clermont-Ferrand, France, University of Clermont-Ferrand, 62 p.
- 746 Bossière, G., Bonkougou, I., Peucat, J.J., Pupin, J.P., 1996. Origin and age of Palaeoproterozoic conglomerates
747 and sandstones of the Tarkwaian Group in Burkina Faso, West Africa. *Precambrian Research* 80, 153-
748 172.
- 749 Bourassa, Y., 2003. Wassa Geology Report: Golden Star Resources Ltd, internal report, 34p;
- 750 Brenan, J.M., Cherniak, D.J., Rose, L.A., 2000. Diffusion of osmium in pyrrhotite and pyrite: implications for
751 closure of the Re-Os isotopic system. *Earth Planetary Sciences Letters* 180, 399-413.
- 752 Brugier, O., Bosch, D., Caby, R., Monié, P., 2013. Timing of Palaeoproterozoic events in the Birimian of the
753 West African Craton. Unpublished report, Module 1.5, Final Report P934A- West African Exploration
754 Initiative-Stage 2, 924p.

- 755 McCuaig, EC., Hronsky JMA. 2014. The mineral system concept: the key to Exploration targeting, Society of
756 Economic Geologists, Inc., Special Publication 18, 153-175.
- 757 Carignan, J., Hild, P., Mévelles, G., Morel, J., Yeghicheyan, D., 2001. Routine analyses of trace elements in
758 geological samples using flow injection and low pressure on-line liquid chromatography coupled to
759 ICP-MS: a study of reference materials BR, DR-N, UB-N, AN-G and GH. *Geostandards Newsletter* 25,
760 187-198.
- 761 Champion, DC., Sheraton, JW., 1997. Geochemistry and Nd isotope systematics of Archaean granites of the
762 Eastern goldfields, Yilgarn Craton: Implications for crustal growth processes. *Precambrian Research* 83,
763 109-132.
- 764 Cardon, O., Reisberg, L., André-Mayer, AS., Leroy, J., Milu, V., Zimmermann, C., 2008. Re-Os systematics of
765 pyrite from the Bolcana porphyry copper deposit, Apuseni Mountains, Romania. *Economic Geology*
766 103, 1695-1702.
- 767 Colvine, AC., Fyon, JA., Heather, KB., Marmont, S., Smith, PM., Troop, DG., 1988. Archaean Lode Gold
768 Deposits in Ontario. Ontario Geological Survey, Miscellaneous Paper 139, 136 p.
- 769 Connolly, J.A.D., 2005. Computation of phase equilibria by linear programming: A tool for geodynamic
770 modeling and its application to subduction zone decarbonation. *Earth and Planetary Science Letters*
771 236, 524-541.
- 772 Connolly, J.A.D., 2009. The geodynamic equation of state: what and how. *Geochemistry, Geophysics,*
773 *Geosystems* 10:Q10014 DOI:10.1029/2009GC002540.
- 774 Cox, K.G., Bell, J.D., Pankhurst, R.J., 1979. The interpretation of igneous rocks. Allen & Unwin 464p.
- 775 Craw, D., Koons, P.O., 1989. Tectonically induced hydrothermal activity and gold mineralisation adjacent to
776 major fault zones. *Economic Geology Monograph* 6, 471-478.
- 777 Creaser, R.A., White, A.J.R., 1991. Yardea-Dacite-Large volume, high-temperature felsic volcanism from the
778 Middle Proterozoic of South Australia. *Geology* 19, 48-51.
- 779 Davis, D.W., Hirdes, W., Schaltegger, E., Nunoo, E.A., 1994. U/Pb age constraints on deposition and
780 provenance of Birimian and goldbearing Tarkwaian sediments in Ghana, West Africa. *Precambrian*
781 *Research* 67, 89-107.
- 782 Davis, J., Miller, J., Thébaud, N., McCuaig, T.C., Jessel, M., Begg, G., Hein, K., Baratoux, L., 2015. Craton-
783 scale lithostratigraphic correlation as an insight for the geodynamic evolution of the SWAC,
784 *Proceedings 13th SGA Biennial Meeting* 4, 1587-1590.

- 785 Debat, P., Nikiéma, S., Mercier, A., Lompo, M., Béziat, D., Bourges F, Roddaz M, Salvi S, Tollon F,
786 Wenmenga U, (2003) A new metamorphic constraint for the Eburnean orogeny from Paleoproterozoic
787 formations of the Man shield (Aribinda and Tampilga countries, Burkina Faso). *Precambrian Res*
788 123:47-65
- 789 Dioh, E., Béziat, D., Debat, P., Grégoire, M., Ngom, P.M., 2005. Diversity of the Palaeoproterozoic granitoids of
790 the Kédougou inlier (Eastern Sénégal): Petrographical and geochemical constraints. *Journal of African*
791 *Earth Sciences* 44, 351-371.
- 792 Doumbia, S., Pouclet, A., Kouamelan, A., Peucat, J.J., Vidal, M., Delor, C., 1998. Petrogenesis of juvenile-type
793 Birimian (Paleoproterozoic) granitoids in Central Cote-d'Ivoire, West Africa: Geochemistry and
794 geochronology. *Precambrian Research* 87, 33-63.
- 795 Drummond, M.S., Defant, M.J. 1990. A Model for trondhjemite-tonalite-dacite genesis and crystal growth via
796 slab melting: Archean to modern comparisons. *Journal of Geophysical Research* 95, 503-521.
- 797 Doublier, M.P., Thébaud, N., Wingate, M.T.D., Romano, S.S., Kirkland, C.L., Gessner, K., Mole, D.R., Evans,
798 N., 2014. Structure and timing of Neoproterozoic gold mineralization in the Southern Cross district
799 (Yilgarn Craton, Western Australia) suggest leading role of late Low-Ca I-type granite intrusions.
800 *Journal of Structural Geology* 67(B), 205-221.
- 801 Egal, E., Thiéblemont, D., Lahondère, D., Guerrot, C., Costea, C.A., Iliescu, D., Delor, C., Goujou, J.C., Lafon,
802 J.M., Tegye, M., 2002. Late Eburnean granitization and tectonics along the western and northwestern
803 margin of the Archean Kenema- Man domain (Guinea West African Craton). *Precambrian Research*
804 117, 57-84.
- 805 Eglinger, A., Thébaud, N., Davis, J., Miller, J., Zeh, A., McCuaig C, Belousova E (2015) High-K to shoshonitic
806 magmatism across the northern Archean Kéména Man margin (Guinea): Implications for the Eburnean
807 orogenic gold mineralizations. *Mineral Resources in a sustainable world. Proceedings 13th SGA Biennial*
808 *Meeting 4:1591-1594*
- 809 Feybesse, J.L., Milési, J.P., 1994. The Archean/Proterozoic contact zone in West Africa: a mountain belt of
810 décollement thrusting and folding on a continental margin related to 2.1 Ga convergence of Archean
811 cratons? *Precambrian Research* 69,199-227.
- 812 Feybesse, J.L., Billa, M., Guerrot, C., Duguey, E., Lescuyer, J.L., Milesi, J.P., Bouchot, V., 2006. The
813 paleoproterozoic Ghanaian province: Geodynamic model and ore controls, including regional stress
814 modeling. *Precambrian Research* 149, 149-196.

- 815 Frimmel, H.E., 2008, Earth's continental crustal gold endowment. *Earth and Planetary Science Letters* 267, 44-
816 55.
- 817 Fu, B., Touret, J.L.R., 2014, From granulite fluids to quartz-carbonate megashear zones: The gold rush.
818 *Geoscience Frontiers* 5, 747-758.
- 819 Ganne, J., De Andrade, V., Weinberg, R., Dubacq, B., Vidal, O., Kagambega, N., Naba, S., Baratoux, L., Jessell,
820 M., Allibone, J., 2011. Modern-style plate subduction pre-served in the Palaeoproterozoic West African
821 Craton. *Nature Geosciences* 5, 60-65.
- 822 Ganne, J., Gerbault, M., Block, S., 2014. Thermo-mechanical modeling of lower crust exhumation-Constraints
823 from the metamorphic record of the Palaeoproterozoic Eburnean orogeny, West African Craton.
824 *Precambrian Research* 243, 88-109.
- 825 Gasquet, D., Barbey, P., Adou, M., Paquette, J.L., 2003. Structure, Sr-Nd isotope geochemistry and zircon U-Pb
826 geochronology of the granitoids of the Dabakala area (Côte d'Ivoire): evidence for a 2.3 Ga crustal
827 growth event in the Palaeoproterozoic of West Africa. *Precambrian Research* 127, 329-35.
- 828 Goldfarb, R.J., Groves, D.I., Gardoll S., 2001. Orogenic gold and geologic time: a global synthesis. *Ore Geology*
829 *Reviews* 18, 1-75.
- 830 Goldfarb, R., Baker, T., Dubé, B., Groves, D.I., Hart, C.J.R., Gosselin, P., 2005. Distribution, Character, and
831 Genesis of Gold Deposits in Metamorphic Terranes. *Economic Geology* 100th Anniversary Volume
- 832 Groves, D.I., Goldfarb, R.J., Robert, F., Hart, C.J.R., 2003. Gold deposits in Metamorphic Belts: Overview of
833 Current Understanding, Outstanding Problems, Future Research and Exploration Significance.
834 *Economic Geology* 98, 1-29.
- 835 Hammarstrom JM, Zen E (1986) Aluminium in hornblende: an empirical igneous geobarometer. *American*
836 *Mineralogist* 71:1297-1313
- 837 Hein, K.A.A., 2010. Succession of structural events in the Goren greenstone belt (Burkina Faso): implications
838 for West African tectonics. *Journal of African Earth Sciences* 56, 83-94.
- 839 Henry, D.J., Guidotti, C.V., Thomson, J.A., 2005. The Ti-saturation surface for low-to-medium pressure
840 metapelitic biotites: Implications for geothermometry and Ti-substitution mechanisms. *American*
841 *Mineralogist* 90, 316-328.
- 842 Hirdes, W., Davis, D.W., Eisenlohr, B.N., 1992. Reassessment of Proterozoic granitoid ages in Ghana on the
843 basis of U/Pb zircon and monazite dating. *Precambrian Research* 56, 89-96.

- 844 Hirdes, W., Davis, D.W., Lüdtke, G., Konan, G., 1996. Two generations of Birimian (Paleoproterozoic) volcanic
845 belts in northeastern Côte d'Ivoire (West Africa): consequences for the «Birimian controversy».
846 *Precambrian Research* 80, 173-191.
- 847 Hirdes, W., Davis, D.W., 1998. First U-Pb zircon age of extrusive volcanism in the Birimian Supergroup of
848 Ghana/West Africa. *Journal of African Earth Sciences* 27, 291-294.
- 849 Holland, T. J. B. and Powell, R., 1998. An internally consistent thermodynamic data set for phases of
850 petrological interest. *Journal of Metamorphic Geology*, 16, 309-343.
- 851 Hollister LS, Grisson GC, Peters EK, Stowell HH, Sisson VB (1987) Confirmation of the empirical correlation
852 of Al in hornblende with pressure of solidification of calc-alkaline plutons. *American Mineralogist*
853 72(34):231-239
- 854 Hottin G, Ouedraogo OF (1976) Carte géologique de la République de Haute-Volta. Direction de la Géologie et
855 des Mines, Ouagadougou, 1 feuille, notice 58 p
- 856 Hottin G, Ouedraogo OF (1992) Carte géologique du Burkina Faso, BRGM/Bureau des Mines et de la Géologie
857 du Burkina, Ouagadougou, 1 feuille, notice 58 p
- 858 Johnson, M.C., Rutherford, M.J. 1992. Experimental calibration of the aluminum-in-hornblende geobarometer
859 with application to Long Valley caldera (California). *Geology* 17, 837-841.
- 860 Kerrich R, Goldfarb R, Groves D, Garwin D (2000) The geodynamic of world-class gold deposits:
861 characteristics, space-time distribution and origins, in Hagemann SG, Brown PE (eds) *Gold in 2000*.
862 Society of Economic Geologists, Reviews in Econ Geol 13:501-551
- 863 Klockner, I.A., 1991. Cartographie géologie du sillon de Téra, Etude géochronologique. Unpublished report,
864 Ministry of Mines and Energy of Niger, Niamey 49-59.
- 865 Koons, P.O., Craw, D., 1991. Gold mineralization as a consequence of continental collision: an example from
866 the Southern Alps, New Zealand. *Earth Planetary Sciences Letters* 103, 1-9.
- 867 Kretschmar, U., Scott, S.D., 1976. Phase relations involving arsenopyrite in the system Fe-As-S and their
868 application. *The Canadian Mineralogist* 14, 364-3.
- 869 Lambert-Smith, J.S., Lawrence D.M., Müller W., Treloar P.J., 2016a, Palaeotectonic setting of the south-eastern
870 Kédougou-Kéniéba Inlier, West Africa: New insights from igneous trace element geochemistry and U-
871 Pb zircon ages, *Precambrian Research* 274, 110-135.

- 872 Lambert-Smith, J.S., Lawrence, D.M., Vargas, C.A., Boyce, A.J., Treloar, P.J., The Goukoto Au deposit, West
873 Africa: Constraints on ore genesis and volatile sources from petrological, fluid inclusion and stable
874 isotope data, *Ore Geology Reviews* 78, 606-622.
- 875 Lanari, P., Wagner, T., Vidal, O., 2014. A thermodynamic model for di-trioctahedral chlorite from experimental
876 and natural data in the system MgO-FeO-Al₂O₃-SiO₂-H₂O: applications to P-T sections and
877 geothermometry. *Contributions to Mineralogy and Petrology* 167, 968.
- 878 Large, R.R., Bull, S.W., Maslennikov, V., 2011. A carbonaceous sedimentary source-rock model for Carlin-type
879 and orogenic gold deposits. *Economic Geology and the Bulletin of the Society of Economic Geologists*
880 106, 331-358.
- 881 Lawley, C.J.M., Selby, D., Condon D.J., Horstwood M., Millar, I., Crowley Q., Imber J., 2013.
882 Litho geochemistry, geochronology and geodynamic setting of the Lupa Terrane, Tanzania: implications
883 for the extent of the Archean Tanzanian Craton, *Precambrian Research* 231, p. 174-193.
- 884 Lawley C.J.M. m McNicoll V., Sandeman H., Pehrsson S., Simard M., Castonguay S., Mercier-Langevin P.,
885 Dubé B., 2016. Age and geological setting of the Rankin Inlet greenstone belt and its relationships to
886 the gold endowment of the Meliadine gold district, Nunavut, Canada. *Precambrian Research* 275, p.
887 471-495.
- 888 Lawrence, D.M., Treolar, P.J., Rankin AH, Harbidge P, Holliday J (2013) The geology and mineralogy of the
889 Loulo mining district, Mali, West Africa: Evidence for two distinct styles of orogenic gold
890 mineralization. *Econ Geol* 108:199-227.
- 891 Le Métour, J., Chèvremont. P., Donzeau, M.E., Thiéblemont, E., Tegey, D., Guerrot, M.C., Itard, B., Castaing,
892 Y., Delpont, C., Ki, G., Zunino, J.C.C., 2003. Notice explicative de la Carte géologique du Burkina
893 Faso à 1/200,000. Feuille Houndé 82p.
- 894 Le Mignot, E., 2014, Les gisements d'or comme témoins de l'histoire géologique du craton ouest-africain :
895 Apports de la datation
- 896 Le Mignot, E., Siebenaller, L., Béziat, D., André-Mayer, A-S., Reisberg, L., Salvi, S., Vélasquez, G.,
897 Zimmermann, C., Naré, A., 2016a. The Paleoproterozoic copper-gold deposit at Gaoua, Burkina Faso:
898 Superposition of orogenic gold on porphyry copper mineralization. *Economic Geology*, accepted
- 899 Le Mignot, E., Reisberg, L., André-Mayer, A-S., Bourassa, Y., John, M., 2016b. Re-Os geochronological
900 evidence for multiple Paleoproterozoic gold events at the scale of the West African craton. *Economic*
901 *Geology*, accepted.

- 902 Leube, A., Hirdes, W., Mauer, R., Kesse, G.O. 1990. The early proterozoic birimian supergroup of Ghana and
903 some aspects of its associated gold mineralization. *Precambrian Research* 46, 139-165.
- 904 Lindgren, W. 1933. *Mineral deposits*. 4th ed New York McGraw-Hill, 930p.
- 905 Lompo, M., 1991. Etude structurale et géologique des séries birimiennes de la région de Kwademen, Burkina
906 Faso, Afrique de l'Ouest. Doctorat de l'université de Clermont Ferrand, France 192p.
- 907 Lompo, M., 2009. A model of subsidence of an oceanic plateau magmatic rocks in the Man-Leo Shield of the
908 West African Craton Geodynamic evolution of the 2.25–2.0 Ga Palaeoproterozoic. In: Reddy SM,
909 Mazumder R, Evans DAD, Collins AS (Eds) *Palaeoproterozoic Supercontinents and Global Evolution*.
910 Geological Society London 231-254.
- 911 Lüdtke, G., Hirdes, W., Konan, G., Kone, Y., Yao, C., Diarra, S., Zamble, Z., 1998, *Géologie de la région Haute*
912 *Comoé Nord avec carte géologique 1/100,000. Feuilles Kong. 4B, 4d, et Tehini-Bouna 3a–3d. Bulletin.*
913 *No. 1 DG Abidjan, p. 178.*
- 914 Lüdtke, G., Hirdes, W., Konan, G., Koné, Y., N'Da, D., Traoré, Y., Zamblé, Z.B., 1999. *Géologie de la région*
915 *haute comoé sud. Carte géologique à 1/100000, feuilles dabakala 2b,d et 4b,d - 1ère édition. Projet de*
916 *coopération géologique ivoiro-allemande cgia (1995-1996). Ministère des Ressources Minières et*
917 *Pétrolières, Direction de la Géologie, Bulletin n°2.*
- 918 Lü, L., Mao, J., Li, H., Pirajno, F., Zhang, Z., Zhou, Z., 2011. Pyrrhotite Re-Os and SHRIMP zircon U-Pb dating
919 of the Hongqiling Ni-Cu sulfide deposits in Northeast China. *Ore Geology Reviews* 43, 106-119.
- 920 Markey, R., Stein, H.J., Hannah, J.L., Zimmerman, A., Selby, D., Creaser, R.A., 2007, *Standardizing Re-Os*
921 *geochronology: a new molybdenite Reference Material (Henderson, USA) and the stoichiometry of Os*
922 *salts. Chemical Geology* 244, 74-87.
- 923 Martin, H., Smithies, R.H., Rapp, S., Moyen, J.F., Champion, D., 2005. An overview of adakite, tonalite-
924 trondhjemite-granodiorite (TTG), and sanukitoid: relationships and some implications for crustal
925 evolution. *Lithos* 79, 1-24.
- 926 Mathur, R., Titley, S., Ruiz, J., Gibbins, S., Frieauf K., 2005. A Re-Os isotope study of sedimentary rocks and
927 copper-gold ores from the Ertsberg District, West Papua, Indonesia. *Ore Geology Reviews* 26, 207-226.
- 928 McDonough, W.F., Sun, S.S., 1995, *The Composition of the Earth. Chemical Geology* 120, 223-253.
- 929 McFarlane, C.R.M., Mavrogenes, J., Lentz, D., King, K., Allibone, A., Holcombe, R., 2011. *Geology and*
930 *Intrusion-Related Affinity of the Morila Gold Mine, Southeast Mali. Economic Geology* 106, 727-750.

- 931 McCuaig, C., Miller, J., Parra, L., Hein, K., Jessell, M., Davis, J., 2014, Craton to Regional-scale analysis of the
932 Birimian of West Africa, *Precambrian Research*, Volume 274, March 2016, Pages 1-2
- 933 McCuaig, T. C., & Hronsky, J. M. (2014). The mineral system concept: the key to exploration targeting. *Society*
934 *of Exploration Geologists Special Publication*, 18, 153-175.
- 935 Metelka, V., Baratoux, L., Naba, S., Jessell, WM., 2011. A geophysically constrained litho-structural analysis of
936 the Eburnean greenstone belts and associated granitoid domains, western Burkina Faso. *Precambrian*
937 *Research* 190, 48-69.
- 938 Milesi, J.P., Feybesse, J.L., Ledru, P., Dommange, A., Ouedraogo, M.F., Marcoux, E., Prost, A., Vinchon, Ch.,
939 Sylvain, J.P., Johan, V., Tegye, M., Calvez, J.Y. and Lagny, P. 1989. West African gold deposits in
940 their Lower Proterozoic lithostructural setting. *Chroniques Recherche Min* 497, 98 pp.
- 941 Milesi, JP., Ledru, P., Feybesse, JL., Dommange, A., Marcoux, E., 1992. Early Proterozoic ore deposits and
942 tectonics of Birimian orogenic belt, West Africa. *Precambrian Research* 58, 305-344.
- 943 Milesi JP, Feybesse JL, Pinna P, Deschamps Y, Kampunzu H, Muhongo S, Lescuyer JL, Le Goff E, Delor C,
944 Billa M, Ralay F, Henry C (2004) Geological map of Africa 1:10,000,000. SIGAfrique project. In: 20th
945 Conference of African Geology, BRGM, Orléans, France, 2-7 June <http://www.sigafrique.net>
- 946 Naba, S., Lompo, M., Debat, P., Bouchez, JL., Béziat, D., 2003. Structure and emplacement model for late-
947 orogenic Paleoproterozoic granitoids: the Tenkodogo-Yamba elongate pluton (Eastern Burkina Faso).
948 *Journal of African Earth Sciences* 38, 41-57.
- 949 Naba, S., 2007. Propriétés magnétiques et caractères structuraux des granites du Burkina Faso oriental (Craton
950 Ouest African, 2.2-2.0Ga) : implications géodynamiques. Doctorat de l'Université de Toulouse, 175p.
- 951 Nesbitt, BE., Murowchick, JB., Muehlenbachs, K., 1986. Dual origins of lode gold deposits in the Canadian
952 Cordillera. *Geology* 14, 506-509.
- 953 Neumayr, P., Ridley, JR., McNaughton, NJ., Kinny, PD., Barley, ME., Groves, DI., 1998. Timing of gold
954 mineralization in the Mt York district: Pilgangoora greenstone belt, and implications for the tectonic
955 and metamorphic evolution of an area linking the western and eastern Pilbara Craton, *Precambrian*
956 *Research* 88, 249-265.
- 957 Nier, A.O. (1937) The isotopic constitution of osmium, *Phys. Rev.* 52, P. 885
- 958 Nier, A.O., 1950. A re-determination of the relative abundances of the isotopes of carbon, nitrogen, oxygen,
959 argon and potassium. *Physical Review.* 77, 789-793.

- 960 Oberthür, T., Vetter, U., Davis, DW., Amanor, JA., 1998. Age constraints on gold mineralization and
961 Paleoproterozoic crustal evolution in the Ashanti belt of southern Ghana. *Precambrian Research* 89,
962 129-143 .
- 963 Parra-Avila, L.A. Belousova, E., Fiorentini, M.L., Baratoux, L., Davis, J., Miller, J., McCuaig, T.C., 2016.
964 Crustal evolution of the Paleoproterozoic Birimian terranes of the Baoulé-Mossi domain, southern West
965 African craton: U-Pb and Hf-isotope studies of detrital zircons. *Precambrian Research* 274, pp. 25-60.
- 966 Perrouy, S., Aillères, L., Jessell, MW., Baratoux, L., Bourassa, Y., Crawford, B., 2012. Revised Eburnean
967 geodynamic evolution of the gold-rich southern Ashanti Belt, Ghana, with new field and geophysical
968 evidence of pre-Tarkwaian deformation. *Precambrian Research* 204-205, 12-39.
- 969 Perrouy, S., Jessell, MW., Bourassa, Y., Miller, J., Apau D., Siebenaller, L., Velasquez, G., Baratoux, L.,
970 Aillères L., Béziat D., Salvi S., 2015. The Wassa deposit: A poly-deformed orogenic gold system in
971 southwest Ghana – Implications for regional exploration, *Journal of African Earth Sciences* 112,536-
972 547.
- 973 Pigois, JP., Groves, DI., Fletcher, IR., McNaughton, NJ., Snee, LW., 2003. Age constraints on Tarkwaian
974 palaeoplacer and lode-gold formation in the Tarkwa-Damang district, SW Ghana. *Mineralium Deposita*
975 38, 695-714.
- 976 Ravenelle, JF., Dubé, B., Malo, M., McNicoll, V., Nadeau, L., Simoneau, J., 2010, Insights on the geology of the
977 world-class Roberto gold deposit, Eléonore property, James Bay area, Québec. *Geological Survey*
978 *Canada, Current Research* 2010-1.
- 979 Reisberg, L., Miesel, T., 2002. The Re-Os isotopic system: A review of analytical techniques. *Geostandards*
980 *Newsletter* 26(3), 249-267.
- 981 Schmidt, MW., 1992. Amphibole composition in tonalite as a function of pressure: an experimental calibration
982 of the Al-in-hornblende barometer. *Contributions to Mineralogy and Petrology* 110, 304-310.
- 983 Selby, D., Creaser, R.A., Hart C.J.R.R., Rombach, C.S., Thompson, J.F.H.H., Smith, M.T., Bakke, A.A.,
984 Goldfarb, R.J., 2002. Absolute timing of sulfide and gold mineralization: a comparison of Re–Os
985 molybdenite and Ar–Ar mica methods from the Tintina Gold Belt, Alaska. *Geology* 30, 791–794.
- 986 Selby, D., Creaser, RA., 2004. Macroscale NTIMS and microscale LA-MC-ICP-MS Re-Os isotopic analysis of
987 molybdenite: Testing spatial restrictions for reliable Re-Os age determinations, and implications for the
988 decoupling of Re and Os within molybdenite. *Geochimica Cosmochimica Acta* 68(19), 3897-3908.

- 989 Sibson, R.H., Robert, F., Poulsen, K.H., 1988. High-angle reverse faults, fluid-pressure cycling, and mesothermal
990 gold-quartz deposits. *Geology* 16: 551-555
- 991 Siegfried, P., De Kock, G.S., Clarke, B., Agenbacht, A., Delor, C., Van Rooyen, R.C., 2009. Geological map
992 explanation – map sheet 0903D (1:100 000): Mining Sector Support Programme. CGS, BRGM,
993 Geoman, GSD, Accra
- 994 Simard, M., 2011. Multi évènements de déformation, de métamorphisme, d’hydrothermalisme à l’origine du
995 gisement Lapa, Thèse de doctorat de l’Université du Québec à Chicoutimi
- 996 Siméon, Y., Delor, C., Vidal, M., Chiron, J.C., Zeade, J., 1992. Mise en évidence d’un épisode tectonique tardi-
997 éburnéen en Côte d’Ivoire. *Comptes rendus RST, Toulouse. Société Géologique de Paris*, p142
- 998 Smoliar, M.I., Walker, R.J., Morgan, J.W., 1996. Re-Os ages of group IIA, IIIA, IVA and IVB iron meteorites:
999 *Science*, vol. 271, p.1099-1102.
- 1000 Stein, H.J., Morgan, J.W., Scherstén, A., 2000. Re-Os dating of Low-Level Highly Radiogenic sulfides: The
1001 Harnäs gold deposit, southwest Sweden, records continental-scale tectonic events. *Economic Geology*
1002 95, 1657-1671.
- 1003 Tapsoba B, Lo CH, Jahn BM, Chung SL, Wenmenga U, Iizuka Y (2013) Chemical and Sr–Nd isotopic
1004 compositions and zircon U–Pb ages of the Birimian granitoids from NE Burkina Faso, West African
1005 Craton: implications on the geodynamic setting and crustal evolution. *Precambrian Research* 224, 364-
1006 396.
- 1007 Taylor, P.N., Moorbath, S., Leube, A., Hirdes, W., 1992. Early Proterozoic crustal evolution in the Birimian of
1008 Ghana: constraints from geochronology and isotope geochemistry. *Precambrian Research* 56, 97-111.
- 1009 Thomas, E., De Kock, G.S., Baglow, N., Viljoen, J., Siaka, Z., 2009. Geological map explanation—map sheet
1010 0903D (1:100,000). CGS/BRGM/Geoman. Geological Survey Department of Ghana (GSD)
- 1011 Tomkins, A.G., Mavrogenes, J.A., 2002. Mobilization of gold as a polymetallic melt during pelite anatexis at the
1012 Challenger gold deposit, South Australia: a metamorphosed Archean deposit. *Economic Geology* 97,
1013 1249-1271.
- 1014 Tshibubudze, A., Hein, K.A.A., Marquis, P., 2009. The Markoye shear zone in NE Burkina Faso. *Journal of*
1015 *African Earth Sciences* 55, 245-256.
- 1016 Tshibubudze, A., Hein, K.A.A., 2013. Structural setting of gold deposits in the Oudalan-Gorouol volcano-
1017 sedimentary belt east of the Markoye shear zone, West African Craton, *Journal of African Earth*
1018 *Sciences* 80, 31-47.

- 1019 Tshibubudze A, Hein KAA (2015) Gold mineralization in the Essakane goldfield in Burkina Faso, West African
1020 craton. *Ore Geology Reviews* Rev, in press.
- 1021 Van Achterbergh E, Ryan CG, Jackson SE, Griffin WL (2001) Data reduction software for LA-ICP-MS:
1022 appendix. In: Sylvester PJ (ed) *Laser ablation-ICP-mass spectrometry in the earth sciences: principles*
1023 *and applications*. Mineralogical Association of Canada, Ottawa, pp 239–243
- 1024 Vegas N, Naba S, Bouchez JL, Jessell M (2007) Structure and emplacement of granite plutons in the
1025 Palaeoproterozoic crust of Eastern Burkina Faso: rheological implications. *International Journal of*
1026 *Earth Sciences (Geol Rundsch)* 97, 1165-1180.
- 1027 Vidal, M., Delor, C., Pouclet, A., Siméon, Y., Alric, G., 1996. Evolution géodynamique de l'Afrique de l'Ouest
1028 entre 2,2 Ga et 2 Ga: le style "archéen" des ceintures vertes et des ensembles sédimentaires birimiens du
1029 nord-est de la Côte-d'Ivoire. *Bulletin de la Société Géologique de France* 167(3), 307-319.
- 1030 Völkening, J., Walczyk, T., Heumann, KG, 1991. Osmium isotope ratio determinations by negative thermal
1031 ionization mass spectrometry. *International Journal of Mass Spectrometry and Ion Processes* 105:147-
1032 159
- 1033 Weatherley D.K., Henley R.W., 2013. Flash vaporization during earthquakes evidenced by gold deposits.
1034 *Nature Geoscience* 6, 294-298.
- 1035 Yavuz, F. 2007. WinAmphcal: A Windows program for the IMA-04 amphibole classification. *Geochem*
1036 *Geophys Geosys* 8:1
- 1037 Yavuz, F., Yavuz, V., Sasmaz, A. 2006. WinClastour-a Visual Basic program for tourmaline formula calculation
1038 and classification. *Computers & Geosciences* 32, 1156-1168

1 **Table captions**

2

3 Table 1: Major element composition of whole-rock samples analyzed by ICP-OES and traces
4 elements composition analyzed by ICP-MS. N: Normalization on chondrite (McDonough and
5 Sun, 1995). Samples from the Tenkodogo-Yamba batholith (T15, DD17) is analyzed by Naba
6 et al., 2003 while basement (TC97) is from Vegas et al., 2008. Finally, Morila diorites
7 samples are from McFarlane et al., 2011.

8

9 Table 2: Representative chemical composition of chlorite generations and thermometry from
10 the ore zones and host rocks, by electron microprobe analysis

11

12

13 Table 3: Mineral analyses of amphibole grains from the Kiaka diorite (KDH337 44.1 and
14 KDH337 69.6) by electron microprobe analyses; P1, P2, P3 and P4 refer to four
15 geobarometers (Hammarstrom and Zen, 1986; Hollister et al., 1987; Johnson and Rutherford,
16 1989 and Schmidt, 1992) and mineral calculation is performed using WinAmphCal (Yavuz et
17 al., 2007).

18

19 Table 4: Representative chemical composition of metamorphic assemblage of the garnet-
20 orthopyroxene-bearing schist by electron microprobe analysis.

21

22 Table 5: Representative EDS analyses of ore-bearing phases in main ore bodies and alteration
23 haloes at Kiaka.

24

25

26 Table 6: Representative chemical composition of biotite generations from the ore zones and
27 host rocks by electron microprobe analysis

28

29 Table 7: Representative chemical composition of tourmaline associated with early
30 mineralization phase in sedimentary and volcanic protoliths. Note that stoichiometry is
31 calculated using the WinClastour software (Yavuz et al., 2006); calculated from the
32 normalization schemes used by the program; T, Z, Y and W refer to site positions.

33

34 Table 8: U-Pb LA-ICP-MS data for the diorite KDH337-105.5 m¹.

35

36 Table 9: Re-Os data for pyrrhotites from assemblages in quartz-biotite metagreywacke,

37

38

Table 1

| Location | The Kiaka deposit | | | Tenkodogo | DD17 | Fada-N'Gourma | Morila | Morila | |
|------------------------------------|-------------------|------------|---------------|-------------|-----------|---------------|----------|----------|--------|
| Sample | KDH291-56.2 | KDH75-64.9 | KDH348-44.5 | KDH337-44.1 | T15 | FC97 | MANU-125 | MANU-126 | |
| Rock type | volcanic rock | schist | metagreywacke | diorite | granitoid | granitoid | diorite | diorite | |
| Oxides / wt. % | | | | | | | | | |
| SiO ₂ | 34.88 | 78.01 | 71.66 | 57.32 | 59.21 | 55.96 | 60.49 | 57.70 | 61.30 |
| TiO ₂ | 0.84 | 0.03 | 0.53 | 0.75 | 0.69 | 0.68 | 0.63 | 0.64 | 0.50 |
| Al ₂ O ₃ | 16.62 | 13.55 | 15.14 | 16.59 | 16.14 | 17.54 | 17.98 | 15.80 | 16.40 |
| Fe ₂ O ₃ | 15.30 | 0.98 | 3.66 | 7.38 | 5.99 | 7.04 | 5.29 | 7.97 | 6.86 |
| MnO | 0.26 | 0.03 | 0.03 | 0.11 | 0.08 | 0.08 | 0.07 | 0.13 | 0.12 |
| MgO | 10.46 | <L.D. | 0.97 | 3.90 | 3.41 | 4.36 | 2.75 | 5.18 | 4.01 |
| CaO | 9.55 | 0.56 | 0.77 | 6.57 | 5.59 | 7.27 | 5.69 | 6.64 | 5.16 |
| Na ₂ O | 0.73 | 4.84 | 1.76 | 3.75 | 4.36 | 4.03 | 4.68 | 2.31 | 1.87 |
| K ₂ O | 3.61 | 1.41 | 1.85 | 1.97 | 2.11 | 1.48 | 1.38 | 2.16 | 2.72 |
| P ₂ O ₅ | 0.19 | <L.D. | 0.14 | 0.27 | 0.34 | 0.29 | 0.28 | 0.38 | 0.19 |
| LOI | 6.12 | 0.86 | 2.74 | 1.53 | 1.00 | 1.02 | 0.69 | - | - |
| Total | 98.56 | 100.27 | 99.24 | 100.14 | 98.92 | 99.75 | 99.93 | 98.91 | 99.13 |
| K ₂ O/Na ₂ O | 4.93 | 0.29 | 1.05 | 0.53 | 0.48 | 0.37 | 0.29 | 0.94 | 1.45 |
| A/CNK | 1.20 | 1.99 | 3.46 | 0.82 | 0.82 | 0.82 | 1.53 | 1.42 | 1.68 |
| Mg# | 0.41 | - | 0.21 | 0.55 | 0.57 | 0.59 | 0.34 | 0.39 | 0.37 |
| Trace elements / ppm | | | | | | | | | |
| Rb | 107.90 | 48.34 | 44.58 | 51.70 | 66.00 | 52.00 | 84.20 | 5.20 | 5.20 |
| Ba | 1206.00 | 29.20 | 464.20 | 665.00 | 1512.00 | 521.00 | 649.00 | 1.00 | 864.00 |
| Nb | 1.39 | 20.32 | 4.16 | 4.29 | 9.15 | 4.01 | 3.14 | 14.30 | 5.34 |
| Ta | 0.10 | 2.09 | 0.41 | 0.33 | 0.63 | 0.31 | 0.155 | 0.20 | 0.33 |
| Sr | 472.80 | 92.33 | 243.70 | 748.00 | 817.00 | 510.00 | 1102.00 | 1102.00 | 687.00 |
| Zr | 56.46 | 104.40 | 117.50 | 129.00 | 275.00 | 144.00 | 103.00 | 2.60 | 135.00 |
| Y | 25.83 | 117.20 | 12.57 | 16.00 | 30.30 | 14.50 | 10.40 | 69.80 | 11.90 |
| Hf | 1.59 | 6.89 | 3.54 | 3.30 | 6.00 | 3.50 | 2.50 | 1.50 | 3.00 |
| Ni | 95.87 | <L.D. | 21.53 | 25.20 | 51.00 | 101.00 | 22.50 | 262.00 | 46.60 |
| Cr | 222.00 | 7.78 | 45.77 | 96.10 | 106.00 | 246.00 | 30.30 | 223.00 | 209.00 |
| V | 268.00 | <L.D. | 89.47 | 140.00 | 114.00 | 136.00 | 96.10 | 3836.00 | 189.00 |
| U | 0.38 | 5.70 | 1.24 | 1.15 | 1.30 | 1.07 | 0.33 | 0.24 | 1.13 |
| Th | 0.62 | 10.37 | 2.60 | 3.83 | 1.88 | 2.59 | 0.36 | 12.50 | 4.09 |
| La | 10.65 | 3.90 | 14.72 | 26.20 | 30.70 | 18.40 | 20.70 | 3.60 | 33.30 |
| Ce | 28.74 | 12.56 | 31.87 | 54.50 | 69.90 | 39.00 | 44.10 | 991.00 | 61.30 |
| Nd | 18.69 | 11.45 | 15.76 | 25.30 | 37.30 | 17.60 | 23.40 | 56.5 | 25.00 |
| Sm | 3.86 | 11.45 | 3.16 | 4.63 | 7.17 | 3.55 | 4.25 | 6.90 | 4.11 |
| Eu | 1.12 | 0.12 | 0.85 | 1.34 | 2.01 | 1.15 | 1.36 | 28.60 | 1.20 |
| Gd | 3.81 | 11.76 | 2.62 | 3.72 | 5.65 | 2.87 | 2.98 | 5.30 | 3.67 |
| Dy | 4.14 | 17.20 | 2.32 | 2.91 | 4.90 | 2.49 | 2.06 | 4.60 | 2.32 |
| Er | 2.72 | 10.86 | 1.30 | 1.48 | 2.85 | 1.34 | 0.94 | 0.50 | 1.28 |
| Yb | 3.02 | 11.17 | 1.36 | 1.48 | 2.67 | 1.35 | 0.86 | 2.80 | 1.27 |
| Lu | 0.49 | 1.66 | 0.22 | 0.23 | 0.44 | 0.21 | 0.12 | 1.50 | 0.21 |
| Sr/Y | 18.3 | 0.79 | 19.39 | 47.00 | 27.00 | 35.00 | 106.00 | 15.79 | 57.73 |
| La/Yb | 3.52 | 0.35 | 10.82 | 18.00 | 12.00 | 14.00 | 24.00 | 1.00 | 26.00 |
| Y/Yb | 8.54 | 10.49 | 9.24 | 11.00 | 11.00 | 11.00 | 12.00 | 25.00 | 9.00 |
| (La/Yb) _N | - | - | - | 13.00 | 8.00 | 10.00 | 35.00 | 1.00 | 18.00 |

Table 2

| Sample | KDH291-56.2 | | | | | | | | | | |
|--------------------------------|-------------|-----------|-----------|-----------|--------|--------|--------|--------|--------|--------|--------|
| Analyses | ZM-10-24b | ZM-10-24b | ZM-10-24b | ZM-10-24b | c1-2a | c1-2b | c1-2c | c1-2d | c3-1a | c3-1b | c3-1c |
| Mineral | Ch11 | Ch11 | Ch11 | Ch11 | Ch12 |
| Location | Inc. tur | Inc. tur | Inc. tur | Inc. tur | Matrix |
| Oxides (wt.%) | | | | | | | | | | | |
| SiO ₂ | 27.71 | 25.76 | 26.75 | 26.10 | 26.66 | 26.35 | 26.69 | 26.77 | 26.34 | 25.78 | 26.49 |
| TiO ₂ | 0.06 | 0.01 | 0.04 | 0.13 | 0.04 | 0.02 | 0.04 | 0.01 | 0.00 | 0.03 | 0.05 |
| Al ₂ O ₃ | 18.83 | 18.34 | 18.20 | 19.12 | 21.68 | 21.72 | 21.41 | 21.38 | 21.66 | 20.35 | 21.93 |
| FeO | 24.83 | 24.58 | 24.64 | 25.26 | 20.71 | 20.02 | 20.72 | 20.58 | 20.28 | 20.34 | 20.81 |
| MnO | 0.58 | 0.55 | 0.35 | 0.62 | 0.41 | 0.35 | 0.42 | 0.42 | 0.36 | 0.41 | 0.33 |
| MgO | 14.91 | 15.10 | 15.76 | 14.29 | 18.62 | 18.63 | 19.13 | 18.81 | 18.27 | 18.08 | 18.93 |
| CaO | 0.13 | 0.35 | 0.06 | 0.20 | 0.05 | 0.04 | 0.00 | 0.00 | 0.03 | 0.00 | 0.05 |
| Na ₂ O | 0.02 | 0.09 | 0.07 | 0.03 | 0.04 | 0.09 | 0.00 | 0.03 | 0.03 | 0.00 | 0.01 |
| K ₂ O | 0.66 | 0.08 | 0.11 | 0.00 | 0.00 | 0.07 | 0.13 | 0.09 | 0.03 | 0.08 | 0.07 |
| Σ | 87.73 | 84.86 | 85.98 | 85.75 | 88.21 | 87.29 | 88.54 | 88.09 | 87.00 | 85.07 | 88.67 |
| nOx | 14 | 14 | 14 | 14 | 14 | 14 | 14 | 14 | 14 | 14 | 14 |
| Si | 2.886 | 2.730 | 2.785 | 2.745 | 2.703 | 2.694 | 2.691 | 2.718 | 2.703 | 2.709 | 2.665 |
| Al ^{IV} | 1.109 | 1.269 | 1.212 | 1.244 | 1.294 | 1.305 | 1.306 | 1.282 | 1.297 | 1.288 | 1.331 |
| Al ^{VI} | 1.202 | 1.021 | 1.022 | 1.126 | 1.296 | 1.312 | 1.237 | 1.276 | 1.324 | 1.232 | 1.270 |
| Ti | 0.005 | 0.001 | 0.003 | 0.010 | 0.003 | 0.002 | 0.003 | 0.001 | 0.000 | 0.002 | 0.004 |
| Fe ²⁺ | 1.838 | 1.307 | 1.287 | 1.445 | 1.580 | 1.541 | 1.485 | 1.573 | 1.567 | 1.520 | 1.489 |
| Fe ³⁺ | 0.324 | 0.871 | 0.858 | 0.778 | 0.176 | 0.171 | 0.262 | 0.175 | 0.174 | 0.268 | 0.263 |
| Mn | 0.051 | 0.049 | 0.031 | 0.055 | 0.035 | 0.030 | 0.036 | 0.036 | 0.031 | 0.036 | 0.028 |
| Mg | 2.315 | 2.385 | 2.446 | 2.241 | 2.814 | 2.839 | 2.875 | 2.847 | 2.795 | 2.832 | 2.839 |
| Ca | 0.015 | 0.040 | 0.007 | 0.023 | 0.005 | 0.004 | 0.000 | 0.000 | 0.003 | 0.000 | 0.005 |
| Na | 0.004 | 0.018 | 0.014 | 0.006 | 0.008 | 0.018 | 0.000 | 0.006 | 0.006 | 0.000 | 0.002 |
| K | 0.088 | 0.011 | 0.015 | 0.000 | 0.000 | 0.009 | 0.017 | 0.012 | 0.004 | 0.011 | 0.009 |
| X _{Mg} | 0.56 | 0.65 | 0.66 | 0.61 | 0.64 | 0.65 | 0.66 | 0.64 | 0.64 | 0.65 | 0.66 |

Table 4

| Sample | KDH337 (44.1 and 69.6) | | | | | | | | | |
|--------------------------------|------------------------|---------------|-------------|---------------|---------------|---------------|---------------|---------------|---------------|--------------------|
| Analysis | | c3-1 | c4-3 | c4-4 | c3-3 | c1-3 | c3-2 | c2-5 | c5-1 | |
| Minerals | Plagiolase (n: 5) | Mg-hornblende | Cannilloite | Mg-hornblende | Mg-hornblende | Mg-hornblende | Mg-hornblende | Mg-hornblende | Mg-hornblende | Actinolite (n: 15) |
| Location | core | core | core | core | core | core | core | core | core | rim |
| Oxides (wt.%) | | | | | | | | | | |
| SiO ₂ | 61.57 | 49.22 | 53.01 | 49.60 | 48.90 | 53.97 | 49.40 | 44.18 | 46.79 | 51.82 |
| TiO ₂ | 0.01 | 0.45 | 0.19 | 0.31 | 0.23 | 0.09 | 0.40 | 1.29 | 0.50 | 0.21 |
| Al ₂ O ₃ | 24.45 | 6.18 | 2.19 | 6.25 | 6.77 | 2.00 | 6.53 | 10.32 | 8.84 | 3.62 |
| Cr ₂ O ₃ | - | 0.00 | 0.61 | 0.00 | 0.05 | 0.034 | 0.02 | 0.06 | 0.04 | 0.13 |
| MgO | - | 11.69 | 13.81 | 11.92 | 11.47 | 18.1 | 13.82 | 9.06 | 10.23 | 13.31 |
| CaO | 5.76 | 12.28 | 18.51 | 12.57 | 12.56 | 12.43 | 12.34 | 12.04 | 12.44 | 12.88 |
| MnO | 0.01 | 0.41 | 0.33 | 0.32 | 0.39 | 0.42 | 0.34 | 0.32 | 0.35 | 0.37 |
| FeO | 0.02 | 16.52 | 10.58 | 15.94 | 15.89 | 14.64 | 16.29 | 17.62 | 17.04 | 15.06 |
| Na ₂ O | 8.41 | 0.66 | 0.28 | 0.49 | 0.61 | 0.29 | 0.63 | 0.94 | 0.71 | 0.38 |
| K ₂ O | 0.11 | 0.54 | 0.13 | 0.41 | 0.58 | 0.14 | 0.53 | 1.07 | 0.78 | 0.26 |
| H ₂ O | - | 1.90 | 2.08 | 1.98 | 1.99 | 2.06 | 2.08 | 1.96 | 1.93 | 2.01 |
| F | - | 0.27 | 0.02 | 0.12 | 0.07 | 0.19 | 0.00 | 0.03 | 0.14 | 0.09 |
| Cl | - | 0.00 | 0.00 | 0.01 | 0.01 | 0.01 | 0.01 | 0.01 | 0.02 | 0.01 |
| Σ | 100.62 | 100.18 | 101.83 | 99.98 | 99.54 | 104.43 | 102.42 | 98.95 | 99.92 | 100.13 |
| nOx | | 23 | 23 | 23 | 23 | 23 | 23 | 23 | 23 | 23 |
| Si | 2.60 | 7.44 | 7.76 | 7.493 | 7.42 | 7.33 | 7.171 | 6.79 | 7.08 | 7.72 |
| Al ^{TOT} | 1.21 | | | | | | | | | |
| Al ^{IV} | - | 0.55 | 0.23 | 0.51 | 0.57 | 0.32 | 0.83 | 1.20 | 0.91 | 0.28 |
| Al ^{VI} | - | 0.52 | 0.11 | 0.57 | 0.52 | 0.00 | 0.20 | 0.61 | 0.53 | 0.28 |
| Fe ³⁺ | - | 0.03 | 0.12 | 0.00 | 0.07 | 1.44 | 0.86 | 0.18 | 0.38 | 0.13 |
| Fe ²⁺ | - | 1.95 | 1.1 | 1.92 | 1.87 | 0.00 | 1.09 | 2.01 | 1.79 | 1.69 |
| Mn | - | - | - | - | - | - | - | - | - | - |
| Mg | - | 2.49 | 2.83 | 2.51 | 2.53 | 3.56 | 2.83 | 2.07 | 2.29 | 2.85 |
| Ca | 0.26 | 1.95 | 2.00 | 1.96 | 1.99 | 1.66 | 1.88 | 1.98 | 1.98 | 1.94 |
| Na | 0.68 | - | - | - | - | - | - | - | - | - |
| K | 0.01 | - | - | - | - | - | - | 0.19 | 0.00 | 0.00 |
| OH | - | 1.01 | 1.956 | 1.02 | 1.03 | 1.85 | 1.95 | 1.03 | 1.03 | 1.64 |

| | | | | | | | | | | |
|-----|------|------|-------|------|------|-----------|------|------|------|------|
| XMg | - | 0.55 | 0.721 | 0.56 | 0.57 | 0.95 | 0.72 | 0.51 | 0.56 | 0.63 |
| An | 0.27 | | | | | P1 (kbar) | 1.29 | 5.24 | 3.38 | |
| Ab | 0.72 | | | | | P2 (kbar) | 1.08 | 5.51 | 3.43 | |
| Or | 0.01 | | | | | P3 (kbar) | 0.92 | 4.24 | 2.68 | |
| | | | | | | P4 (kbar) | 1.92 | 5.65 | 3.9 | |

Table 5

| Sample | KDH300 - 470 | | | | | |
|--------------------------------|--------------|-------------|------------------|-------|--------------------------|--------------|
| Mineral | grt (n : 51) | pl (n : 10) | opx (n : 16) | amp | bt ₁ (n : 17) | chl (n : 21) |
| Location | rim-core | core | core | core | core | core |
| Oxides (wt.%) | | | | | | |
| SiO ₂ | 38.47 | 63.43 | 51.84 | 43.26 | 35.69 | 25.39 |
| TiO ₂ | 0.05 | 0.02 | 0.05 | 0.10 | 1.84 | 0.04 |
| Al ₂ O ₃ | 20.42 | 23.88 | 1.306 | 12.75 | 16.13 | 20.73 |
| FeO | 32.77 | 0.13 | 31.12 | 22.17 | 25.19 | 31.52 |
| MnO | 2.60 | 0.03 | 0.92 | 0.30 | 0.13 | 0.34 |
| MgO | 2.41 | 0.00 | 12.12 | 6.31 | 7.94 | 10.82 |
| CaO | 4.44 | 4.64 | 0.53 | 11.21 | 0.16 | 0.05 |
| Na ₂ O | 0.00 | 9.45 | 0.10 | 1.36 | 0.01 | 0.00 |
| K ₂ O | 0.00 | 0.03 | 0.00 | 0.35 | 8.46 | 0.11 |
| Σ | 101.21 | 101.64 | 98.04 | 97.86 | 95.61 | 89.03 |
| nOx | 12 | 8 | 6 | 23 | 22 | 28 |
| Si | 3.05 | 2.11 | 2.05 | 6.59 | 5.55 | 5.43 |
| Ti | 0.00 | 0.00 | 0.00 | 0.01 | 0.21 | 0.01 |
| Al | 1.91 | 1.18 | 0.06 | 2.29 | 2.96 | 5.22 |
| Fe _{tot} | 2.17 | 0.00 | 1.03 | 2.82 | 3.28 | 5.64 |
| Mn | 0.17 | 0.00 | 0.03 | 0.04 | 0.02 | 0.06 |
| Mg | 0.29 | 0.00 | 0.71 | 1.43 | 1.84 | 3.45 |
| Ca | 0.38 | 0.21 | 0.02 | 1.83 | 0.03 | 0.01 |
| Na | 0.00 | 0.77 | 0.01 | 0.40 | 0.00 | 0.00 |
| K | - | 0.00 | 0.00 | 0.40 | 1.68 | 0.06 |
| Σ | 7.98 | 5.12 | 3.92 | 15.49 | 15.58 | 35.94 |
| X _{alm} | 0.72 | | Al ^{IV} | | 2.44 | 2.56 |
| X _{prp} | 0.09 | | Al ^{VI} | | 0.52 | 2.66 |
| X _{grs} | 0.13 | | X _{Fe} | | 0.64 | 0.62 |
| X _{sps} | 0.06 | | X _{Mg} | | 0.36 | 0.38 |
| An | | 0.21 | | | | |
| Ab | | 0.78 | | | | |
| Or | | 0.01 | | | | |

Table 3

| Sample | KDH291-56.2 | | | | | | KDH29-311.8 | | | | | | KDH300-394.5 | |
|--------------------------------|-------------|--------|--------|--------|--------|--------|-------------|--------|--------|--------|--------|--------|--------------|-------|
| Number | c1-2 | c1-4 | c1-8 | c1-10 | 6 | 9 | 14 | 19 | 4 | 17 | 8 | 10 | c6.1 | c3.1 |
| Mineral | Bt2 | Bt2 | Bt2 | Bt2 | Bt1 | Bt1 | Bt1 | Bt1 | Bt2 | Bt2 | Bt2 | Bt2 | Bt1 | Bt3 |
| Location | Matrix | Matrix | Matrix | Matrix | Matrix | Matrix | Matrix | Matrix | Matrix | Matrix | Matrix | Matrix | Matrix | Vein |
| Oxides (wt.%) | | | | | | | | | | | | | | |
| SiO ₂ | 36.93 | 37.03 | 34.86 | 36.39 | 36.54 | 35.10 | 35.09 | 35.77 | 35.67 | 35.29 | 34.84 | 35.70 | 34.31 | 37.41 |
| TiO ₂ | 1.10 | 1.35 | 0.88 | 1.13 | 1.36 | 1.28 | 1.45 | 1.51 | 1.38 | 1.33 | 1.36 | 1.68 | 2.40 | 0.93 |
| Al ₂ O ₃ | 17.98 | 17.51 | 17.83 | 17.69 | 18.00 | 19.28 | 18.71 | 18.19 | 18.65 | 18.34 | 18.72 | 17.89 | 17.67 | 17.59 |
| FeO | 16.42 | 15.39 | 17.63 | 16.62 | 16.57 | 16.98 | 17.00 | 17.18 | 16.60 | 18.31 | 16.37 | 15.82 | 22.55 | 12.72 |
| MnO | 0.17 | 0.18 | 0.26 | 0.19 | 0.19 | 0.31 | 0.27 | 0.17 | 0.32 | 0.28 | 0.23 | 0.18 | 0.43 | 0.93 |
| MgO | 13.60 | 13.70 | 14.42 | 13.66 | 13.01 | 12.18 | 12.06 | 12.20 | 12.05 | 12.19 | 12.50 | 12.52 | 7.46 | 15.85 |
| CaO | 0.04 | 1.83 | 0.02 | 0.09 | 0.00 | 0.02 | 0.00 | 0.01 | 0.00 | 0.00 | 0.03 | 0.04 | 0.00 | 0.00 |
| Na ₂ O | 0.09 | 0.10 | 0.06 | 0.09 | 0.06 | 0.08 | 0.13 | 0.17 | 0.10 | 0.06 | 0.14 | 0.08 | 0.00 | 0.00 |
| K ₂ O | 9.38 | 8.88 | 7.34 | 9.07 | 8.97 | 8.59 | 8.82 | 8.99 | 8.70 | 8.58 | 9.18 | 8.76 | 10.03 | 9.67 |
| Σ | 95.71 | 95.97 | 93.30 | 94.93 | 94.69 | 93.82 | 93.54 | 94.19 | 93.48 | 94.36 | 93.36 | 92.66 | 93.97 | 95.14 |
| nOx | 22 | 22 | 22 | 22 | 22 | 22 | 22 | 22 | 22 | 22 | 22 | 22 | 22 | 22 |
| Si | 5.51 | 5.50 | 5.33 | 5.48 | 5.50 | 5.34 | 5.375 | 5.443 | 5.444 | 5.382 | 5.346 | 5.480 | 5.51 | 5.36 |
| Al ^{IV} | 2.49 | 2.50 | 2.67 | 2.52 | 2.49 | 2.65 | 2.625 | 2.557 | 2.556 | 2.618 | 2.654 | 2.520 | 2.10 | 2.45 |
| Al ^{VI} | 0.67 | 0.56 | 0.55 | 0.62 | 0.69 | 0.81 | 0.754 | 0.706 | 0.799 | 0.679 | 0.733 | 0.718 | 1.14 | 0.59 |
| Ti | 0.12 | 0.15 | 0.10 | 0.13 | 0.15 | 0.14 | 0.167 | 0.173 | 0.158 | 0.153 | 0.157 | 0.194 | 0.28 | 0.10 |
| Fe | 2.05 | 1.91 | 2.26 | 2.09 | 2.08 | 2.16 | 2.178 | 2.186 | 2.119 | 2.335 | 2.101 | 2.031 | 2.95 | 1.58 |
| Mn | 0.02 | 0.02 | 0.03 | 0.02 | 0.02 | 0.04 | 0.035 | 0.022 | 0.041 | 0.036 | 0.030 | 0.023 | 0.05 | 0.10 |
| Mg | 3.02 | 3.03 | 3.29 | 3.07 | 2.92 | 2.765 | 2.753 | 2.767 | 2.741 | 2.770 | 2.859 | 2.864 | 1.74 | 3.48 |
| Ca | 0.01 | 0.29 | 0.00 | 0.01 | 0.00 | 0.003 | 0.000 | 0.002 | 0.000 | 0.000 | 0.005 | 0.007 | 0.00 | 0.00 |
| Na | 0.03 | 0.03 | 0.02 | 0.03 | 0.02 | 0.024 | 0.039 | 0.050 | 0.030 | 0.018 | 0.042 | 0.024 | 0.00 | 0.00 |
| K | 1.78 | 1.68 | 1.43 | 1.74 | 1.72 | 1.670 | 1.724 | 1.745 | 1.694 | 1.669 | 1.797 | 1.716 | 2.00 | 1.81 |
| X _{Mg} | 0.60 | 0.61 | 0.59 | 0.59 | 0.58 | 0.56 | 0.56 | 0.56 | 0.56 | 0.54 | 0.58 | 0.59 | 0.37 | 0.69 |

Table 7

| Sample | KDH29-56.2 | | | | KDH 311.8 | | |
|---------------------------------|------------|--------|--------|--------|-----------|-------|-------|
| | c1.17 | c2.3 | c3.12 | c3.24 | c1.1 | c1.2 | c1.5 |
| Analyses | c1.17 | c2.3 | c3.12 | c3.24 | c1.1 | c1.2 | c1.5 |
| Mineral | tur2 | tur2 | tur2 | tur2 | tur2 | tur2 | tur2 |
| Location | core | core | core | core | core | core | core |
| Oxides (wt%) | | | | | | | |
| SiO ₂ | 35.88 | 36.00 | 35.24 | 35.7 | 36.15 | 36.01 | 35.73 |
| Al ₂ O ₃ | 31.16 | 30.54 | 31.81 | 32.48 | 34.69 | 32.03 | 33.89 |
| TiO ₂ | 0.99 | 1.09 | 0.31 | 0.17 | 0.21 | 0.78 | 0.34 |
| FeO(T) | 5.04 | 5.6 | 4.79 | 5.13 | 4.63 | 5.52 | 4.9 |
| MgO | 9.31 | 9.31 | 8.84 | 8.48 | 7.58 | 8.47 | 7.74 |
| CaO | 1.63 | 1.48 | 0.83 | 0.53 | 1.22 | 1.65 | 1.24 |
| Na ₂ O | 1.96 | 1.91 | 2.16 | 2.08 | 1.59 | 1.5 | 1.57 |
| LiO ₂ * | 0.129 | 0.111 | 0.09 | 0.099 | 0.18 | 0.02 | 0.15 |
| B ₂ O ₃ * | 10.311 | 10.446 | 10.074 | 10.259 | 10.49 | 10.41 | 10.23 |
| H ₂ O* | 3.18 | 3.315 | 3.221 | 3.278 | 3.17 | 3.16 | 3.1 |
| Σ | 95.62 | 97.872 | 93.386 | 95.636 | 96.84 | 96.58 | 94.47 |
| nOx | 24.5 | 24.5 | 24.5 | 24.5 | 24.5 | 24.5 | 24.5 |
| Si ^T | 6.06 | 5.99 | 6.04 | 5.93 | 5.96 | 6.01 | 5.95 |
| Al ^T | 0.00 | 0.01 | 0.00 | 0.07 | 0.04 | 0.00 | 0.05 |
| T Total | 6.068 | 6.00 | 6.038 | 6.00 | 6.00 | 6.01 | 6.00 |
| Al ^Z | 5.96 | 5.873 | 6.00 | 6.00 | 6.00 | 6.00 | 6.00 |
| Mg ^Z | 0.04 | 0.127 | 0.00 | 0.00 | 0.00 | 0.00 | 0.00 |
| Fe ^{3+Z} | 0.00 | 0.00 | 0.00 | 0.00 | 0.00 | 0.00 | 0.00 |
| Z total | 6.00 | 6.00 | 6.00 | 6.00 | 6.00 | 6.00 | 6.00 |
| Al ^Y | 0.00 | 0.00 | 0.303 | 0.319 | 0.6 | 0.3 | 0.56 |
| Ti ^Y | 0.127 | 0.125 | 0.00 | 0.00 | 0.00 | 0.00 | 0.00 |
| Fe ^{2+Y} | 0.564 | 0.696 | 0.577 | 0.708 | 0.55 | 0.7 | 0.57 |

Table 8

| Spot | Element concentrations (ppm) | | | Element Ratio | Radiogenic ratios | | | Rho ^a | Ages (in Ma) | | | %conc ^b | | | | | | |
|------|------------------------------|-----|-----|---------------|-------------------|-------------------------------------|--------|------------------|-------------------------------------|--------|--------------------------------------|--------------------|----|-------------------------------------|----|-------------------------------------|----|-------|
| | Pb | U | Th | | Th/U | ²⁰⁷ Pb/ ²³⁵ U | ± | | ²⁰⁶ Pb/ ²³⁸ U | ± | ²⁰⁷ Pb/ ²⁰⁶ Pb | | ± | ²⁰⁶ Pb/ ²³⁸ U | ± | ²⁰⁷ Pb/ ²³⁵ U | ± | |
| 1 | 256 | 537 | 447 | 0.83 | 7.1871 | 0.0870 | 0.3879 | 0.0046 | 0.98 | 0.1344 | 0.0014 | 2156 | 18 | 2113 | 21 | 2135 | 11 | 99.0 |
| 2 | 196 | 527 | 170 | 0.32 | 6.2539 | 0.0757 | 0.3452 | 0.0041 | 0.98 | 0.1314 | 0.0014 | 2117 | 18 | 1912 | 20 | 2012 | 11 | 95.0 |
| 3 | 118 | 245 | 228 | 0.93 | 7.1888 | 0.0873 | 0.3917 | 0.0046 | 0.97 | 0.1331 | 0.0014 | 2140 | 18 | 2131 | 21 | 2135 | 11 | 99.8 |
| 4 | 190 | 398 | 367 | 0.92 | 7.1747 | 0.0871 | 0.3866 | 0.0046 | 0.97 | 0.1346 | 0.0014 | 2159 | 18 | 2107 | 21 | 2133 | 11 | 99.0 |
| 5 | 275 | 575 | 669 | 1.16 | 6.8155 | 0.0830 | 0.3717 | 0.0044 | 0.97 | 0.1330 | 0.0014 | 2138 | 18 | 2038 | 21 | 2088 | 11 | 97.7 |
| 6 | 207 | 502 | 181 | 0.36 | 6.9958 | 0.0853 | 0.3802 | 0.0045 | 0.97 | 0.1335 | 0.0014 | 2144 | 18 | 2077 | 21 | 2111 | 11 | 98.5 |
| 7 | 106 | 227 | 173 | 0.76 | 7.2281 | 0.0889 | 0.3910 | 0.0046 | 0.96 | 0.1341 | 0.0014 | 2152 | 18 | 2127 | 22 | 2140 | 11 | 99.4 |
| 8 | 198 | 418 | 445 | 1.06 | 6.8509 | 0.0845 | 0.3772 | 0.0045 | 0.97 | 0.1317 | 0.0014 | 2121 | 18 | 2063 | 21 | 2092 | 11 | 98.6 |
| 9 | 261 | 548 | 403 | 0.74 | 7.1623 | 0.0884 | 0.3933 | 0.0047 | 0.96 | 0.1321 | 0.0014 | 2126 | 18 | 2138 | 22 | 2132 | 11 | 100.3 |
| 10 | 249 | 514 | 577 | 1.12 | 7.0208 | 0.0868 | 0.3813 | 0.0045 | 0.96 | 0.1336 | 0.0014 | 2145 | 18 | 2082 | 21 | 2114 | 11 | 98.6 |
| 11 | 190 | 421 | 253 | 0.6 | 7.2622 | 0.0901 | 0.3926 | 0.0047 | 0.96 | 0.1342 | 0.0014 | 2153 | 19 | 2135 | 22 | 2144 | 11 | 99.6 |
| 12 | 174 | 393 | 253 | 0.64 | 7.0616 | 0.0878 | 0.3860 | 0.0046 | 0.96 | 0.1327 | 0.0014 | 2134 | 19 | 2104 | 21 | 2119 | 11 | 99.3 |
| 13 | 178 | 371 | 355 | 0.96 | 7.1479 | 0.0892 | 0.3890 | 0.0046 | 0.96 | 0.1333 | 0.0014 | 2142 | 19 | 2118 | 22 | 2130 | 11 | 99.4 |
| 14 | 197 | 398 | 430 | 1.08 | 7.2038 | 0.0900 | 0.3913 | 0.0047 | 0.96 | 0.1335 | 0.0014 | 2145 | 19 | 2129 | 22 | 2137 | 11 | 99.6 |
| 15 | 200 | 467 | 207 | 0.44 | 7.1787 | 0.0905 | 0.3927 | 0.0047 | 0.95 | 0.1326 | 0.0014 | 2133 | 19 | 2135 | 22 | 2134 | 11 | 100.1 |
| 16 | 212 | 420 | 519 | 1.24 | 7.1801 | 0.0908 | 0.3927 | 0.0047 | 0.95 | 0.1326 | 0.0015 | 2133 | 19 | 2135 | 22 | 2134 | 11 | 100.0 |
| 17 | 197 | 422 | 334 | 0.79 | 2.2262 | 0.0915 | 0.3921 | 0.0047 | 0.95 | 0.1337 | 0.0015 | 2147 | 19 | 2133 | 22 | 2140 | 11 | 99.7 |
| 18 | 334 | 823 | 98 | 0.12 | 7.0293 | 0.0891 | 0.3797 | 0.0046 | 0.95 | 0.1343 | 0.0015 | 2155 | 19 | 2075 | 21 | 2115 | 11 | 98.2 |
| 19 | 217 | 425 | 538 | 1.27 | 7.1652 | 0.0912 | 0.3917 | 0.0047 | 0.94 | 0.1327 | 0.0015 | 2134 | 19 | 2131 | 22 | 2132 | 11 | 99.9 |
| 20 | 189 | 382 | 422 | 1.1 | 7.2337 | 0.0924 | 0.3923 | 0.0047 | 0.94 | 0.1338 | 0.0015 | 2148 | 19 | 2133 | 22 | 2141 | 11 | 99.7 |
| 21 | 258 | 574 | 535 | 0.93 | 6.6133 | 0.0846 | 0.3643 | 0.0044 | 0.94 | 0.1317 | 0.0015 | 2120 | 19 | 2003 | 21 | 2061 | 11 | 97.2 |
| 22 | 135 | 291 | 246 | 0.85 | 7.1474 | 0.0921 | 0.3897 | 0.0047 | 0.93 | 0.1330 | 0.0015 | 2138 | 19 | 2122 | 22 | 2130 | 11 | 99.6 |

^a rho: error correlation of ²⁰⁷Pb/²³⁵U and ²⁰⁶Pb/²³⁸U defined as (err ²⁰⁶Pb/²³⁸U)/(err ²⁰⁷Pb/²³⁵U)

^b Concordance calculated as (²⁰⁷Pb/²³⁵U/²⁰⁷Pb/²⁰⁶Pb)*100

Errors are listed at 1σ

Table 9

| Samples | Minerals | Sample mass (g) | [Re] (ppb) ¹ | ¹⁸⁷ Re (ppb) ^{1,2,3} ± 2σ | Total ¹⁸⁸ Os (ppt) ⁴ | % ¹⁸⁸ Os from blank | Total ¹⁸⁷ Os (ppt) | % ¹⁸⁷ Os * ⁵ | ¹⁸⁷ Os * (ppt) ^{2,5} | ¹⁸⁷ Os*/ ¹⁸⁷ Re ^{1,2,5} ± 2σ | Age (Ma) ^{2,6} ± 2σ | MSWD | ¹⁸⁷ Re/ ¹⁸⁸ Os | ¹⁸⁷ Os/ ¹⁸⁸ Os | rho |
|-------------------------------------|----------|-----------------|-------------------------|---|--|--------------------------------|-------------------------------|------------------------------------|--|---|------------------------------|-------------|--------------------------------------|--------------------------------------|--------|
| KDH280-101b | Po | 0.30387 | 2.33 | 1.46 ± 0.01 | 1.51 | 10 | 54.1 | 98.6 | 53.34 ± 0.62 | 0.0365 ± 0.0007 | 2151 ± 43 | | 1080 ± 123 | 40 ± 5 | 0.9896 |
| KDH280-101c | Po | 0.30696 | 2.48 | 1.56 ± 0.01 | 1.51 | 9 | 58.1 | 98.7 | 57.39 ± 0.63 | 0.0368 ± 0.0007 | 2168 ± 40 | | 1144 ± 130 | 43 ± 5 | 0.9907 |
| KDH280-101d | Po | 0.30047 | 2.37 | 1.49 ± 0.01 | 1.50 | 10 | 55.1 | 98.6 | 54.37 ± 0.63 | 0.0365 ± 0.0007 | 2150 ± 42 | | 1104 ± 126 | 41 ± 5 | 0.9897 |
| sample/deposit weighted mean | | | | | | | | | | | 2157 ± 24 | 0.25 | | | |

¹ Re data are blank corrected.

² All listed uncertainties are 2σ.

³ Uncertainty on ¹⁸⁷Re includes measurement precision, blank uncertainty, weighing errors and uncertainty on spikes calibration.

⁴ Includes both common osmium contained in the sample and the contribution from the blank.

⁵ ¹⁸⁷Os* = ¹⁸⁷Os radiogenic only, calculated assuming a natural osmium ratio of ¹⁸⁷Os/¹⁸⁸Os = 0.5 ± 0.4. Uncertainty on ¹⁸⁷Os* includes the uncertainty on this ratio, measurement precision, weighing errors, uncertainty on spikes calibration and uncertainty on standard measurements.

⁶ Assuming λ¹⁸⁷Re = 1.666 × 10⁻¹¹ yr⁻¹ (Smoliar et al., 1996).

Figure captions

Figure 1: Geology of West African craton (modified after Castaing et al., 2003; Naba et al., 2003, Milesi et al., 2004, Vegas et al., 2008, Ganne et al., 2011). The Kénéma Man domain (Archean nucleus) and the Baoulé-Mossi domain (Paleoproterozoic juvenile crust) form two distinct domains separated by the Sassandra Fault (SF). Volcano-sedimentary belts include Banfora (BA), Houndé (HO), Boromo (BO), Lawra (LW), Goren (GO), Bui (BU), Ashanti (AS) and Sefwi (SW), Haute Comoé basin (HC) and Manga Fada-N’Gourma belt (MFG). These belts are separated into dark green for mafic volcanics rocks and light green for volcano-sedimentary rocks and intermediate to felsic igneous rocks (Baratoux et al., 2011). A spatial association between gold deposits of the Baoulé-Mossi and major structures such as the Grenville-Ferkessedougou-Bobo-Dialouso (GFBF), Ouango-Fitini (OF) and Markoye (MSZ; this study) shear zones is observed in the Baoulé-Mossi domain.

Figure 2: Geology of the Manga-Fada-N’Gourma area with MSZ (thick black lines) and location of the Kiaka gold deposit (compiled after Hottin et Ouédraogo, 1975; Milési et al., 1992; Castaing et al., 2003; Naba et al., 2004 and Vegas et al., 2007).

Figure 3: Local geology of the Kiaka deposit and drillhole and cross-section locations. The KDH300 drillhole was sampled for geochronology, petrographic study and P-T estimation. Mineralized envelopes are projected at surface from drillhole data.

Figure 4: NW-trending cross-sections (A: 6100, B: 5800), plan view and longitudinal section within the Kiaka deposit. The 6100 section illustrates the relationship between the porphyric diorite, metagreywacke rocks and gold mineralization and the 5800 show structural and

lithological control on ore bodies. Plan and longitudinal sections illustrates the contour of inferred pit and the associated gold distribution with potential ore shoots.

Figure. 5: Macroscopic examples of key samples from the Kiaka host rocks. Quartz-muscovite greywacke (A) and lithic greywacke (B) and Aluminosilicate-bearing metapelites (C). The porphyric diorite intrusion (D; KDH337-44.1) is also found at the vicinity of ore shoots. Most of contact between quartz-biotite metagreywacke and metavolcanic rock are strongly altered and deformed but some are locally preserved (E).

Figure 6: Photomicrographs under transmitted light (a, c and d) or crossed polarized light (b) and metamorphic paragenesis with various inferred protoliths. Petrography of less altered host rocks including volcano-sedimentary units (a, b, c) and diorite intrusion (d) associated with the Kiaka gold deposit. Aluminosilicate-bearing metagreywacke (KDH348- 44.5) are located in south footwall of D₂-related shear zones and are locally mineralized (See Fig. 11d for details). A garnet-orthopyroxene-bearing volcano-sedimentary unit (c, KDH300-470) is used to estimate M2 metamorphic peak (for details, see Table 4) probably associated with diorite emplacement (d).

Figure 7: Total alkalis vs. SiO₂ diagram (A) from Cox et al., 1979, spider diagram (B; primitive mantle normalizing values from McDonough and Sun, 1995) and selected REE plot (C; chondritic normalizing values from Sun and McDonough, 1995) for the diorite KDH337-44.1 (Fig. 5F and Fig. 8d and 11f) showing similarities with the Tenkodogo-Yamba batholith samples T15 and DD17 (Naba et al., 2014), the sample FC97 (described as tonalitic basement) of Vegas et al., 2008 and the Morila diorites MANU-125 and MANU-126 (McFarlane et al., 2011).

Figure 8: Photomicrographs of outcrops (A, B, D) and drill core sample (C, E and G). PK₁ folds (A) are more open than isoclinal PK₂ folds (C and G) and appear as relicts preserved from the transposition during D₂ deformation. Specially, those FK₁ folds are observed in metapelites but not in mafic rocks (C). Note that pyrrhotite aggregates (red) are affected by SK₂ foliation (E) and aluminosilicate porphyroblasts (grey) are muscovite-rich and kyanite is also found as relicts. SK₂ shear bands are also observed (D; right side panels are sketches of photographs shown on left side) and are associated LK₂ mineral lineation (B). Example of aluminosilicate-bearing metapelites show (F) evidence of reverse movement along SK₂ shear bands (outcrop location: long. 739288; lat. 1289019; UTM WGS84), and folding (G)

Figure 9: Stereoplot showing the main planar and linear structures within the Kiaka deposit including poles of SK₂ metamorphic foliation (green circles), LK₂ mineral lineation (brown triangles), DK₃₋₄ vein planes (dark and red squares) and FK₁ fold axis (blue squares).

Figure 10: Paragenetic sequence of the Kiaka gold deposit with emphasis on the relationships between mineralization styles (disseminated and vein stages) and hydrothermal assemblages.

Figure 11: Examples of the superposition of hydrothermal alteration within metasedimentary rocks. Photomicrographs of the typical ore style of the disseminated stage composed of a deformed biotite-clinozoisite-pyrrhotite-pyrite-chalcopyrite assemblage hosted by the lithic metagreywacke (A; KDH280-101m; Re-Os sample). DK₃ Hydrothermal breccia in metapelites associated with silicification and actinolite and diopside alteration (B), DK₃ diopside veins associated with epidote-actinolite alteration cuts by DK₄ carbonate veinlets (C). Chlorite-carbonate alteration assemblage with visible gold and electrum in the chlorite sheets

ore within fractured clinozoizite (See Fig. 12 for details) overprinting a biotite-clinozoizite alteration stage (D; KDH29-318.7m). Calcite vein associated with chloritization (Chl_2) cuts a mineralized biotite tourmaline assemblage (E; KDH291-56.2m). Pyrrhotite, chalcopyrite and pyrite are the main sulfides present while biotite aggregates are intergrown with clinozoisites and titanite. Tourmaline contains sulfides, chlorite (Chl_1) and amphibole as inclusions. Sulfides (pyrrhotite and chalcopyrite) are indicated in red (E).

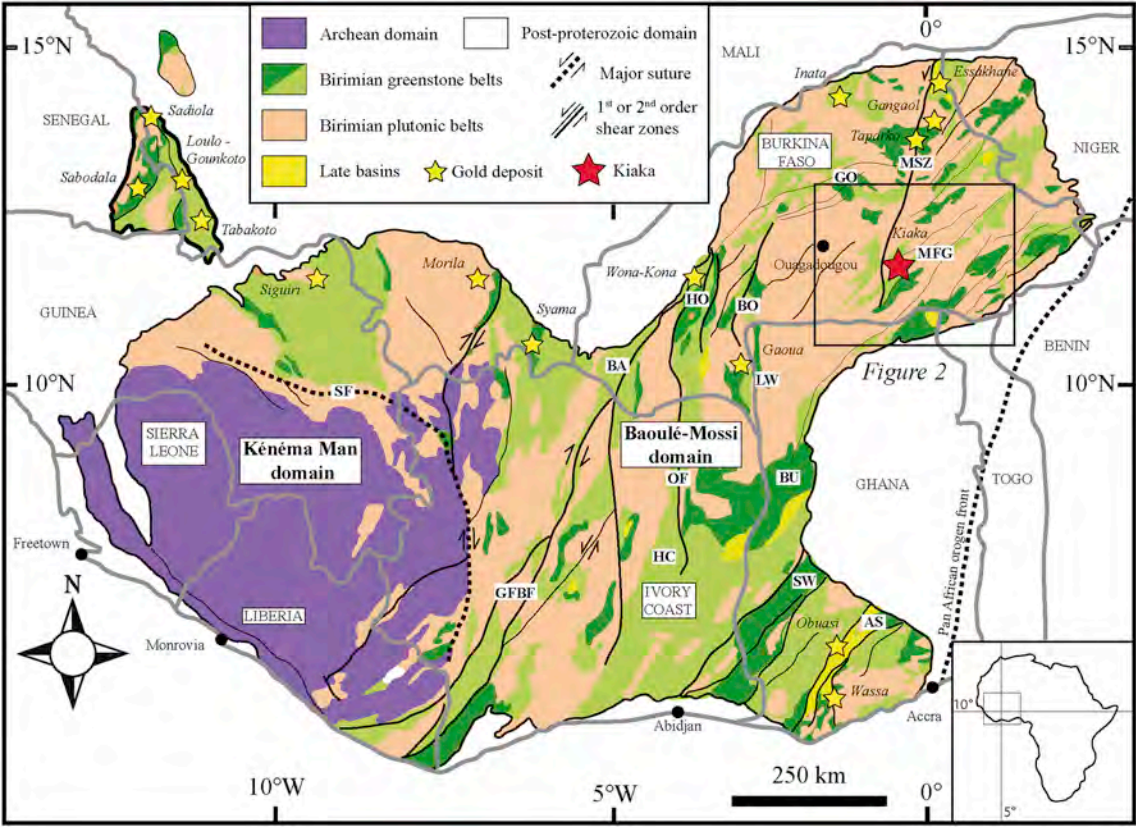
Figure 12: Microphotographs under natural light of pyrrhotite-pyrite-chalcopyrite assemblage in aluminosilicate-bearing pelites (A, KDH348-44.5). Reflected light images of quartz-biotite metagreywacke (B, KDH300-130). Arsenopyrite and lollingite appears to be replaced by pyrrhotite in metapelites (C, KDH348-139). Visible gold is locally found in quartz-carbonates veins within quartz muscovite schist (D, same sample as Fig. 11D). SEM/BSE images of electrum is sometimes associated with arsenopyrite with Co zonation (E) and pyrrhotite found in association with electrum, chalcopyrite and contains inclusions of bismuth telluride (F).

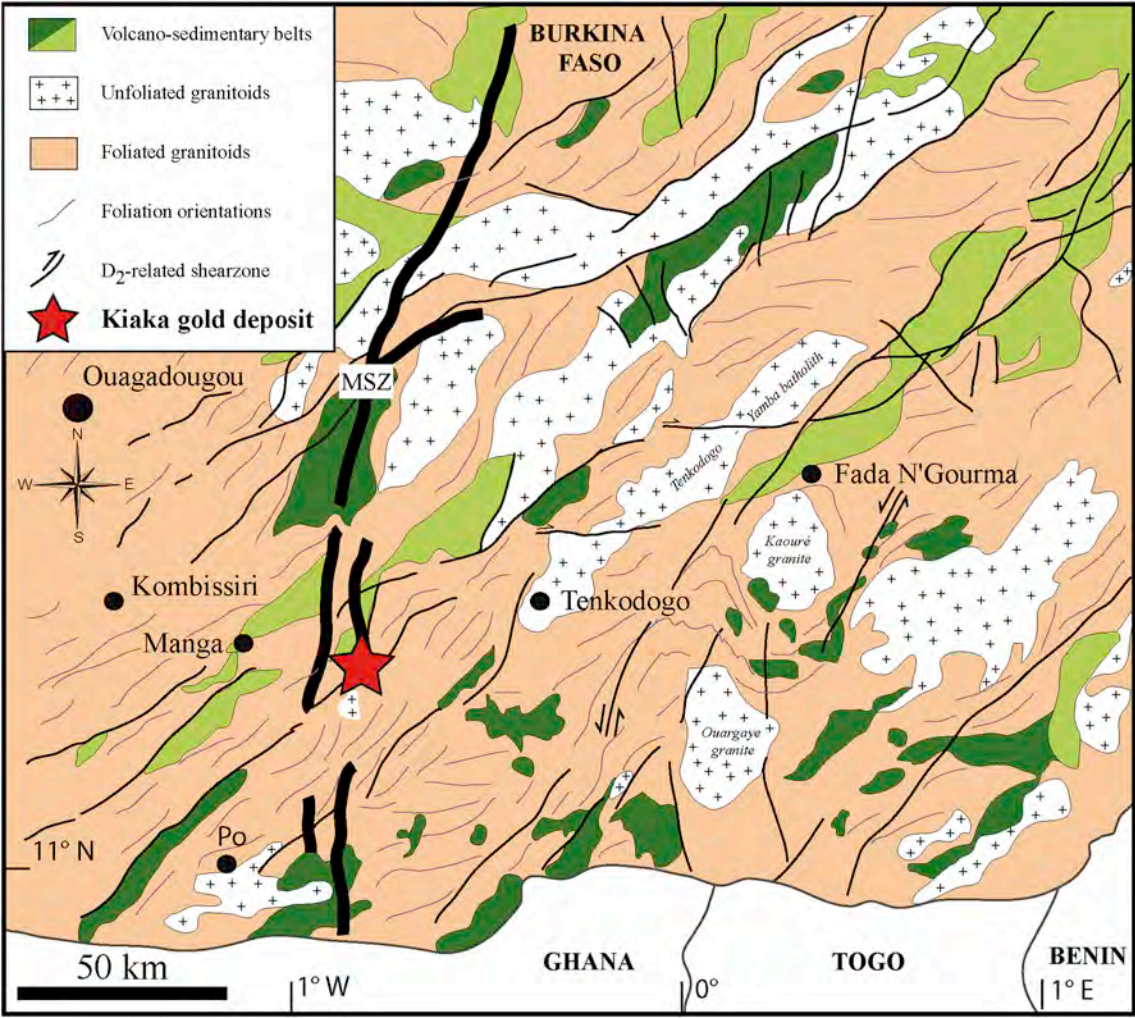
Figure 13: Photomicrographs under natural light (A, B, C and E) or crossed polarized light (D and F). Petrography of hydrothermally altered host rocks including volcano-sedimentary units (A, B, C, D and E) and diorite intrusion (F) associated with the Kiaka gold deposit. Biotitization locally associated with disseminated tourmaline and clinozoizite. Actinolite developed in corona textures around Mg-hornblende (F).

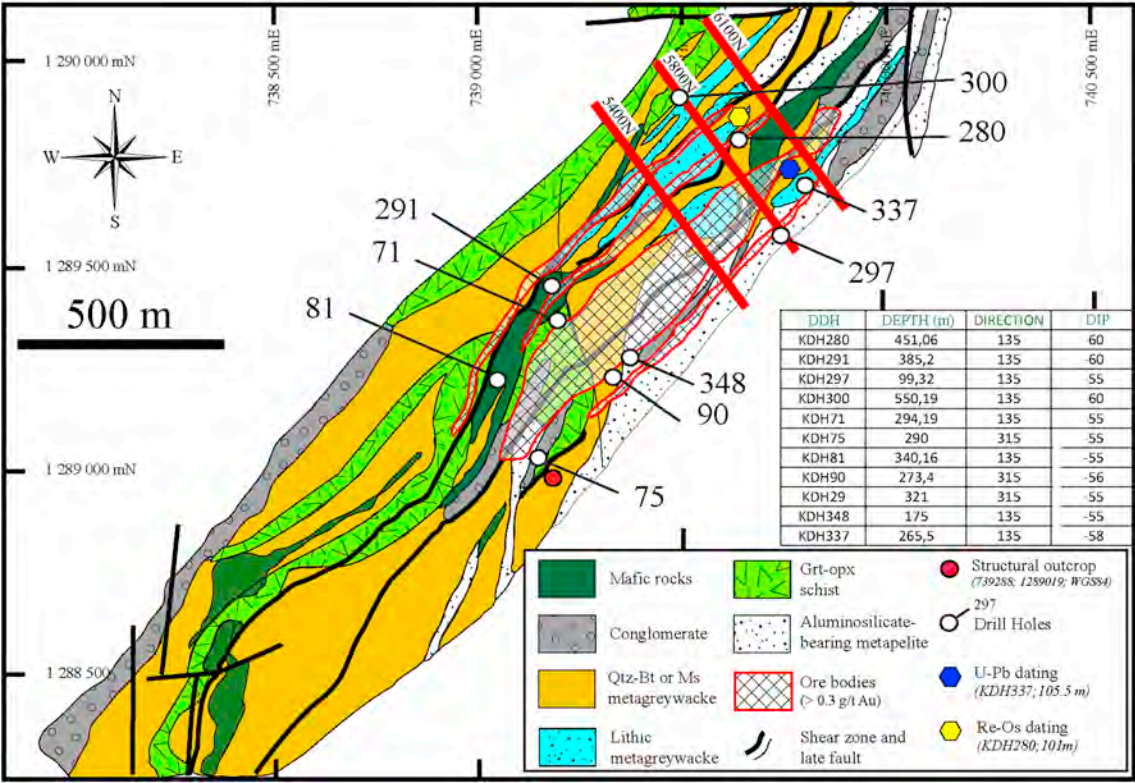
Figure 14: Zircon U-Pb Concordia plot of the sample KDH337 – 105.5 m with examples of subeuhedral zircons within the diorite. See Table 8 for details. TL, transmitted light; CL, cathodoluminescence.

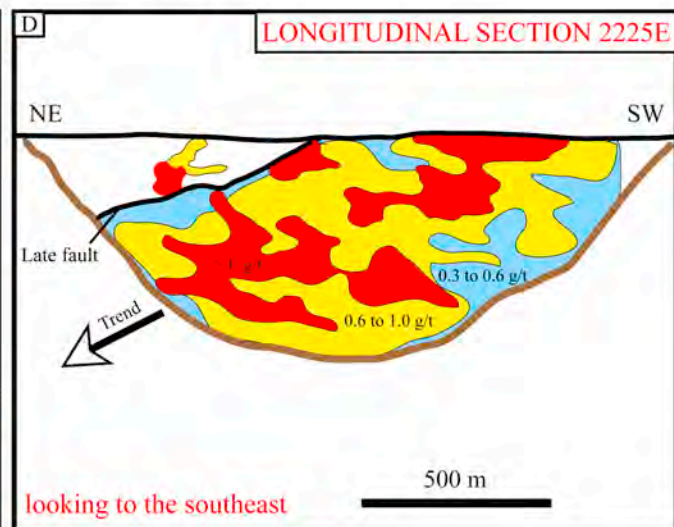
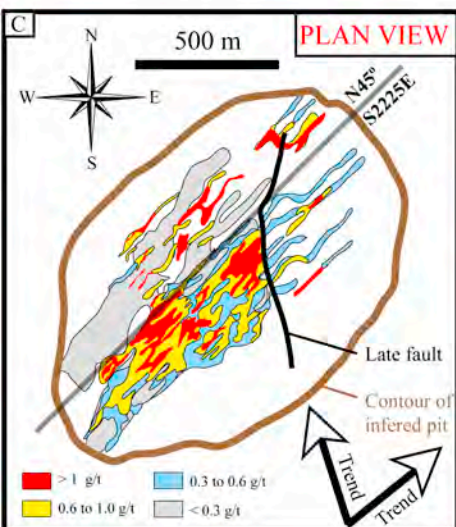
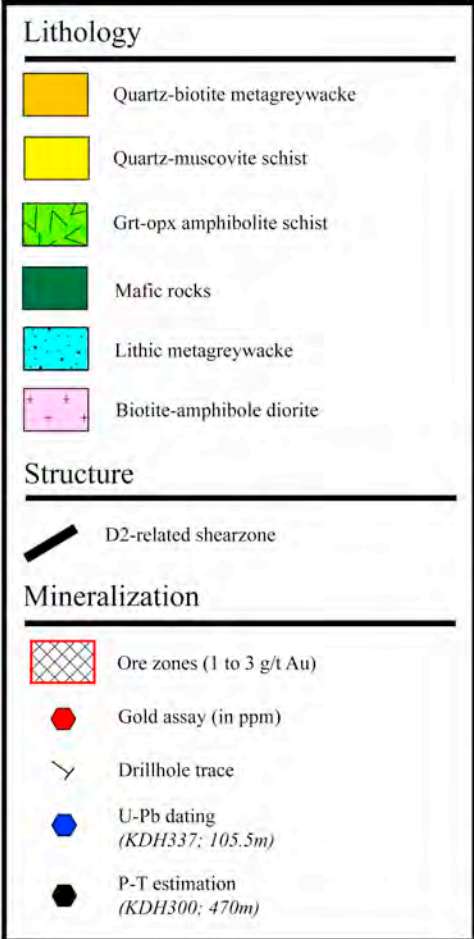
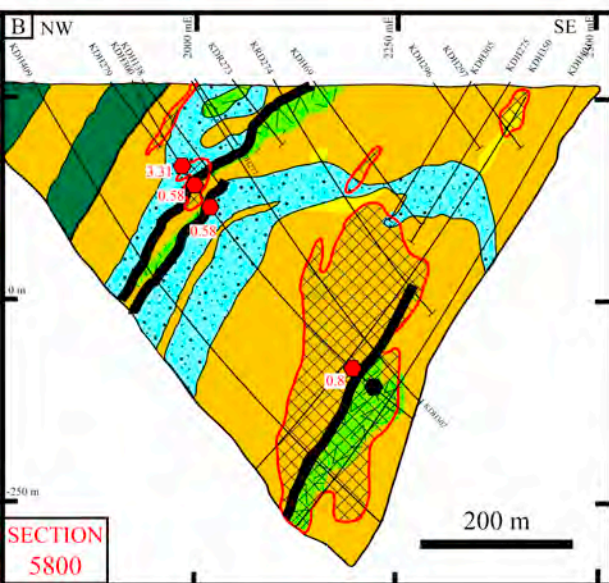
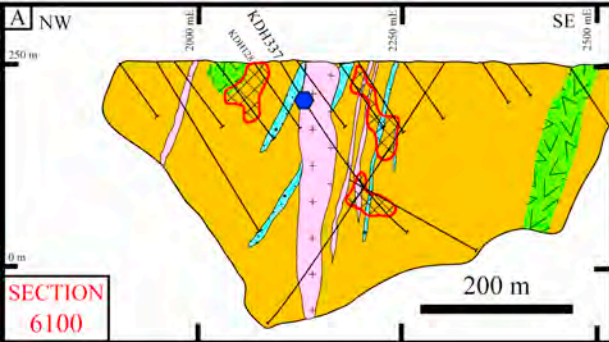
Figure 15: Idealized 3D diagram representing key geological features and P-T diagram with peak metamorphism estimate for the Kiaka area and some recent metamorphic data of the Baoulé-Mossi domain from Ganne et al., 2011 (Manga-Fada-N'Gourma belt), and Block et al., 2015 (northern Ghana).

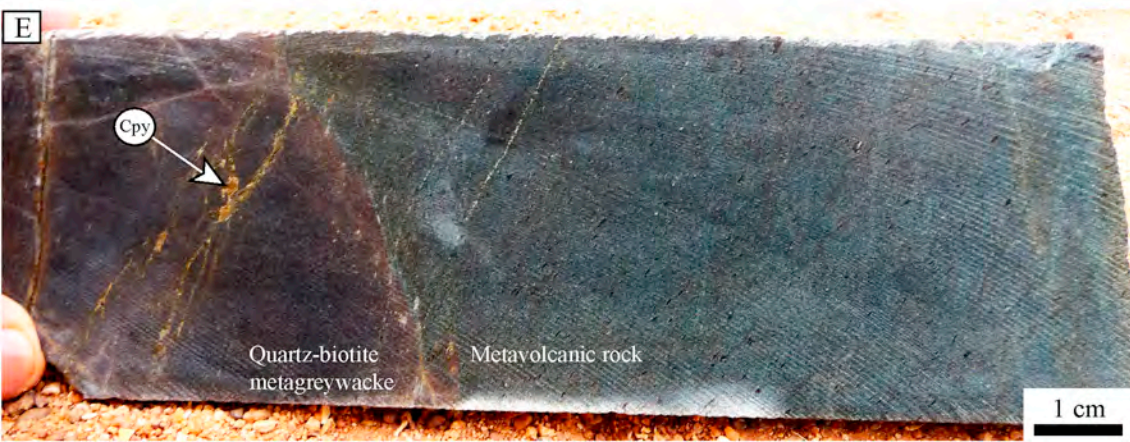
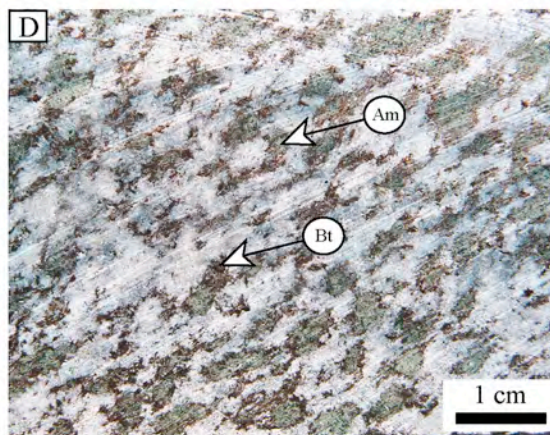
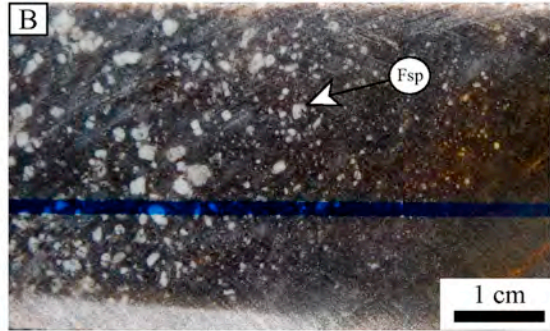
Figure 16: Compilation of the geochronological data for plutonic (light gray symbols) and volcanic (dark gray symbols) magmatic rocks and gold mineralizing events within the Baoulé-Mossi domain placed within the framework of the tectono-metamorphic evolution and magmatic activity of the region. Dark and light gray lines refer to age uncertainties. Age references: (1) Agyei Duodu et al., 2009; (2) Baratoux and Brugier, 2013, unpublished data; (3) Brugier et al., 2013, unpublished data; (4) Castaing et al., 2003; (5) Ennih and Liégeois, 2008; (6) Klockner, 1991; (7) Le Métour et al., 2003; (8) Lompo, 1991; (9) McCuaig et al., 2014, unpublished data ; (10) Ama Salah et al., 1996; (11) Schwartz, 2003; (12) Simeon et al., 1992; (13) Siegfried et al., 2009; (14) Tapsoba et al., 2013; (15) Thomas et al., 2009; (16) Block et al., 2015; (17) Miller et al., 2014, unpublished data; (18) Le Mignot et al. 2016b and (*) this study. Geod., Meta. And Def., respectively, refers to Geodynamic, Metamorphism and Deformation.

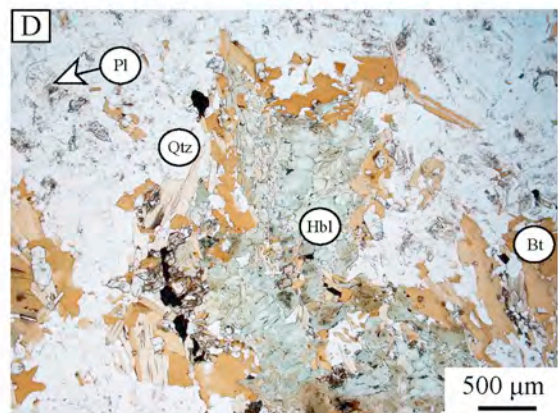
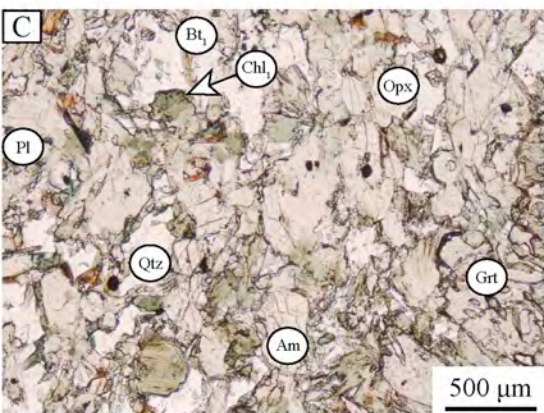
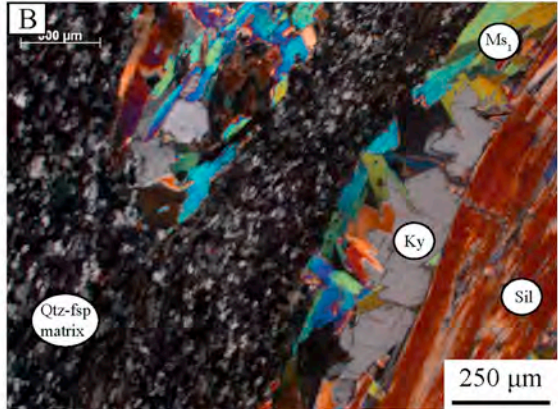
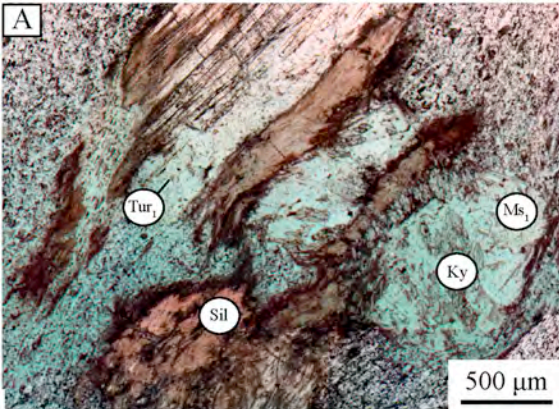






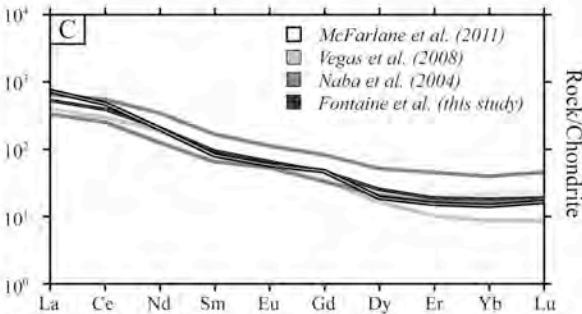
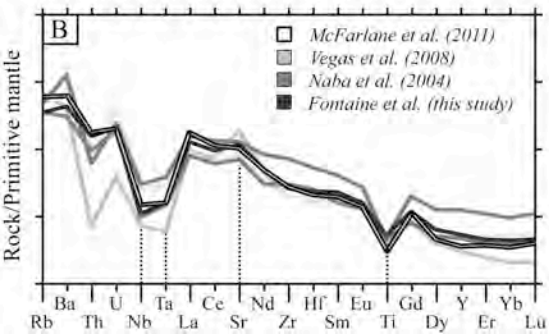
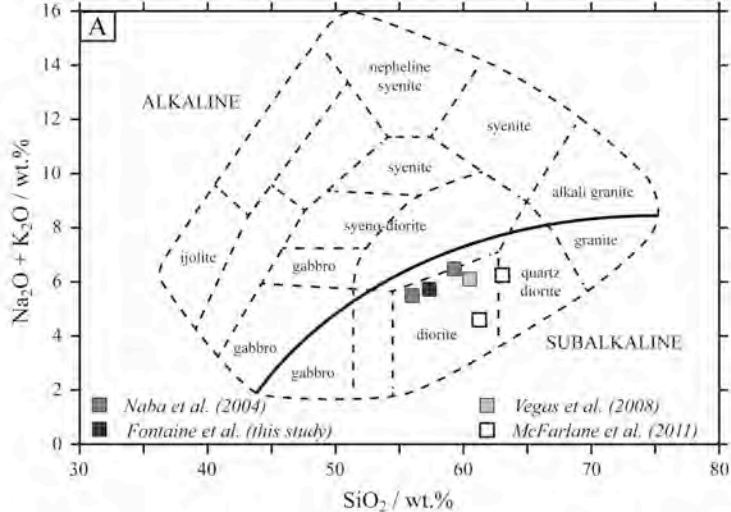


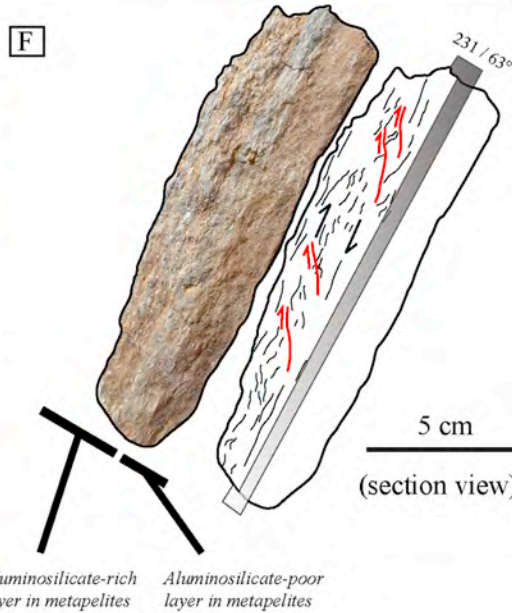
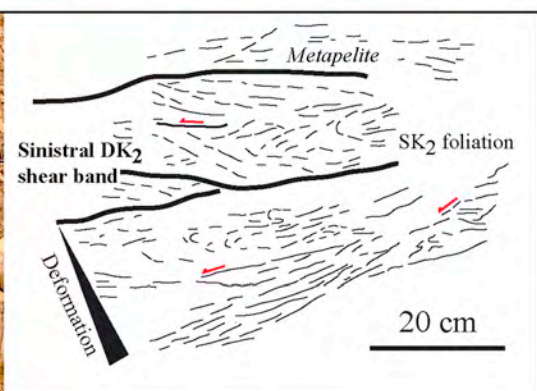
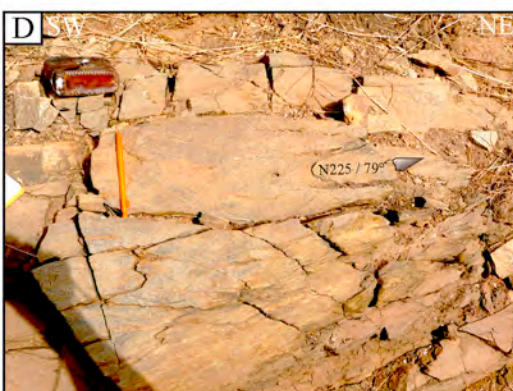




| Protolith type | Minerals | Protolith | DK ₁ event / Prograde metamorphism | DK ₂ event / Prograde metamorphism and diorite emplacement | DK ₁ -DK ₂ events / Retrograde metamorphism during reactivation of D ₂ shear zones |
|----------------|--|---|---|--|--|
| | | | - SK ₂ foliation - PK ₁ open folds | - SK ₂ metamorphic foliation - LK ₂ mineral lineation - PK ₂ isoclinal folds - DK ₂ shear zones | - Sinistral displacement and retrogression within D ₂ -related shear zones - DK ₁ : Hydrothermal breccia - DK ₂ : Chlorite-carbonate veinlets |
| Metasediments | Muscovite Quartz Biotite Kyanite Sillimanite Tourmaline Feldspars | Ms ₁ ————— ————— Tur ₁ ————— ————— | Bt ₁ ————— ————— | Lower amphibolite facies Bt ₂ ————— ————— | Ms ₂ Upper greenschist facies Bt ₁ (vein) ————— Tur ₂ ————— |
| Metabasites | Biotite Tourmaline Feldspars Quartz Orthopyroxene Amphiboles Chlorite Calcite Garnet Ilmenite | Bt ₁ ————— ————— ————— Chl ₁ ————— | | | Bt ₂ ————— ————— Chl ₂ (vein) - - - - - - - - - - |
| Diorite | Mg-Hornblende Quartz Feldspars Biotite Actinolite Calcite Muscovite | ————— ————— ————— ————— | | | ————— - - - - - - - - - - |

————— Major ——— Minor - - - - - Rare

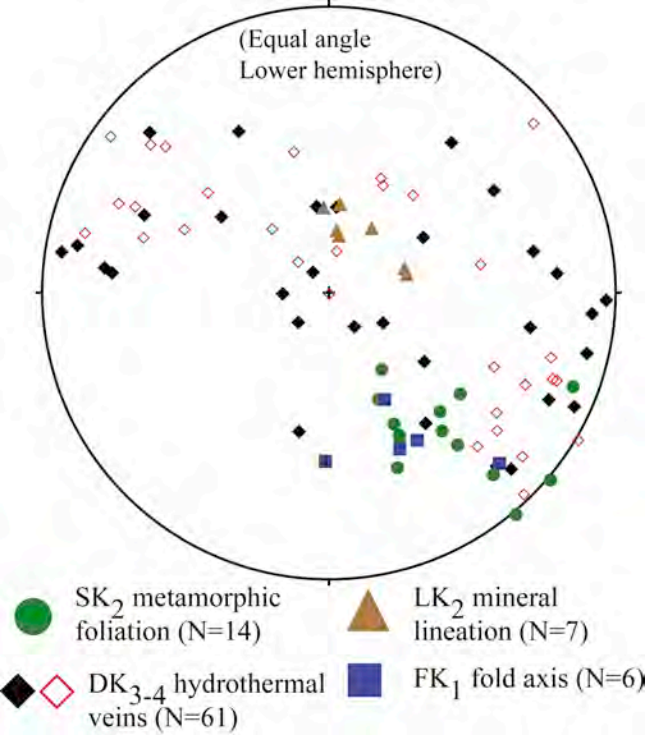




Aluminosilicate-rich layer in metapelites

Aluminosilicate-poor layer in metapelites

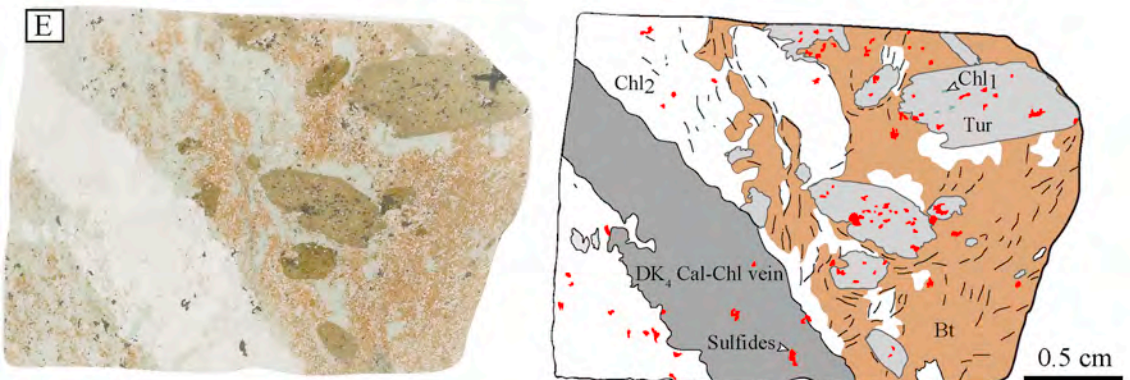
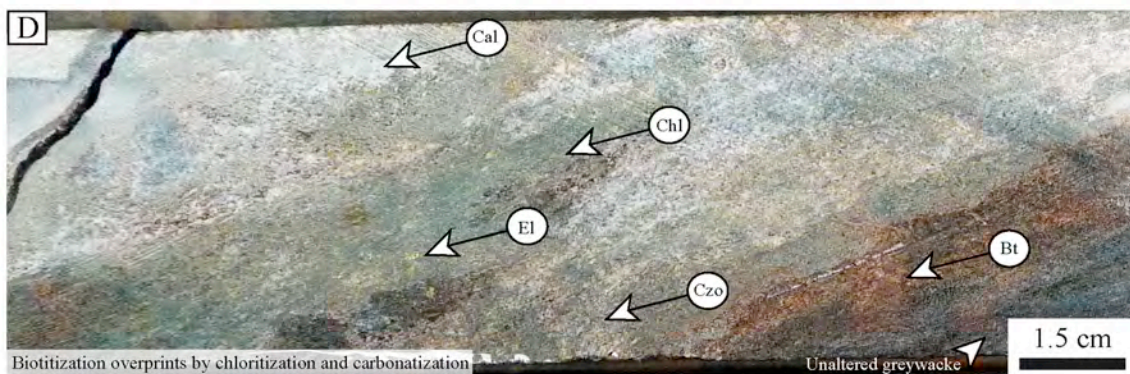
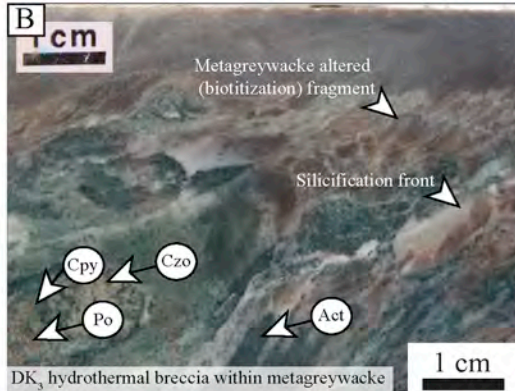
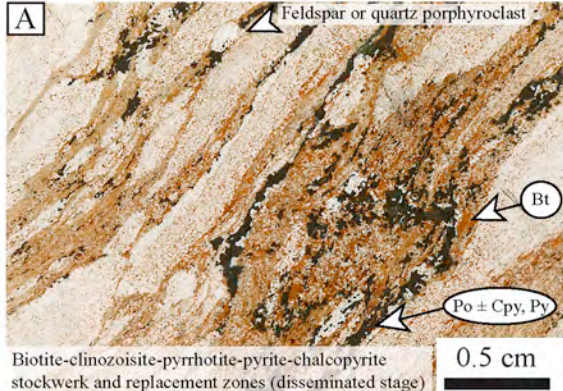
(Equal angle
Lower hemisphere)

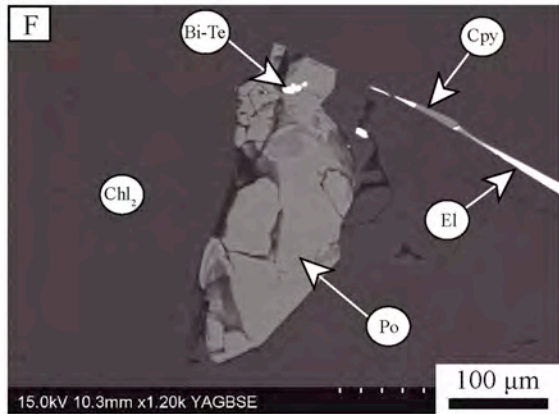
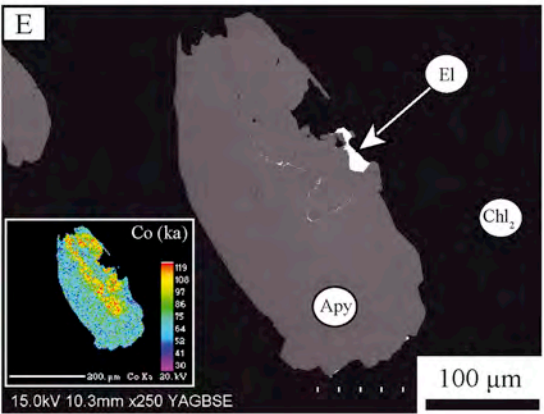
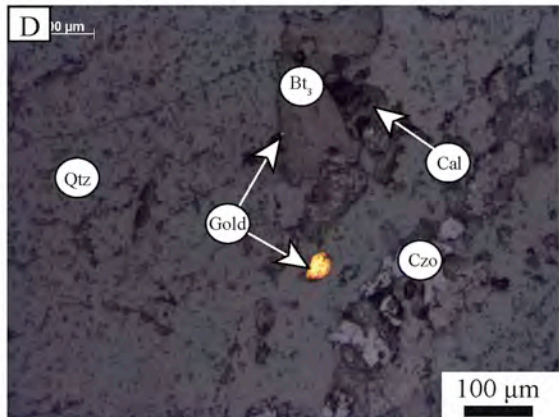
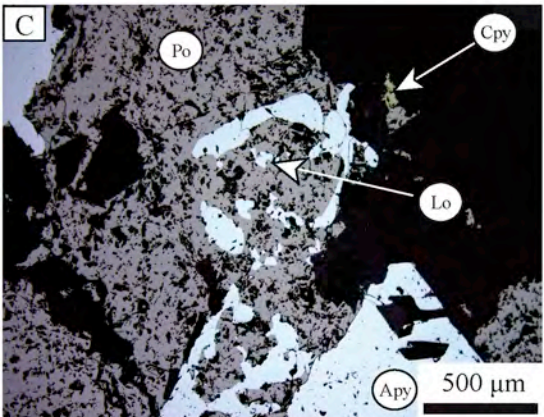
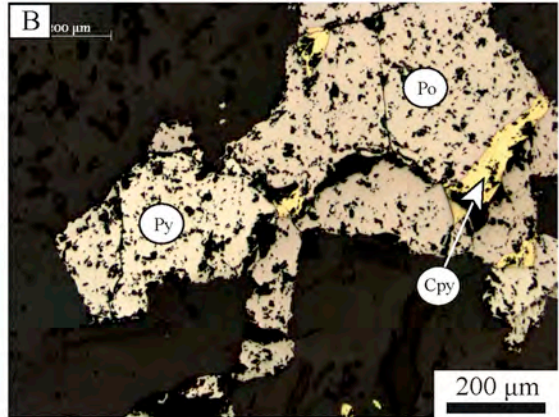
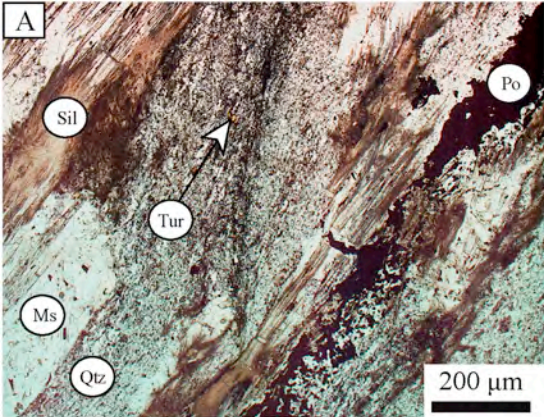


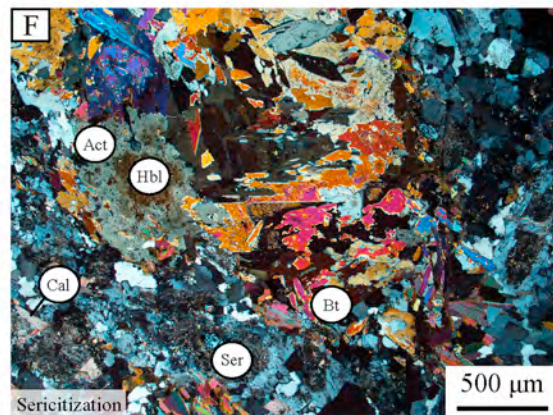
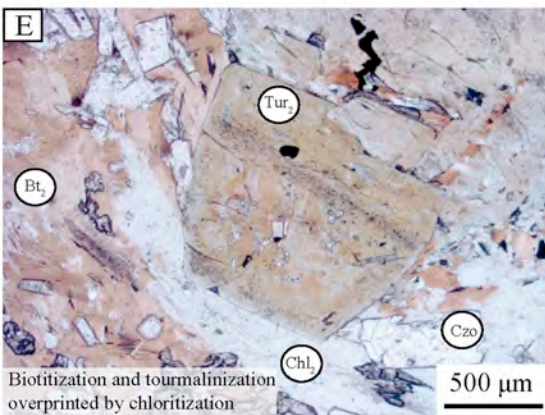
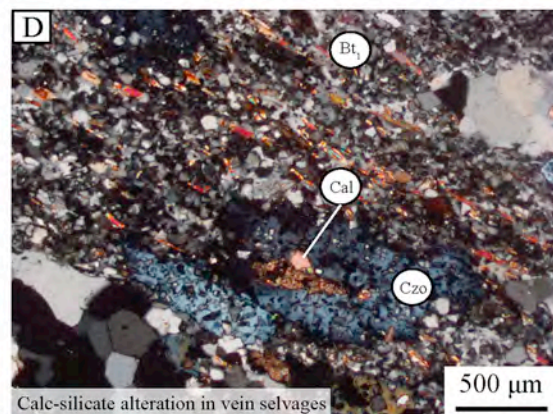
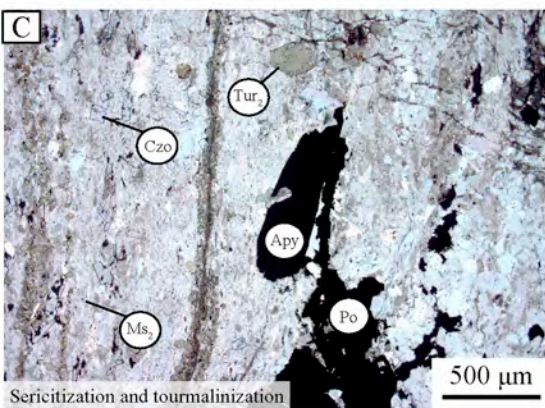
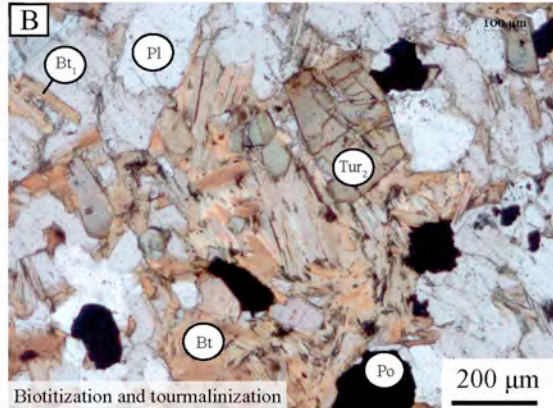
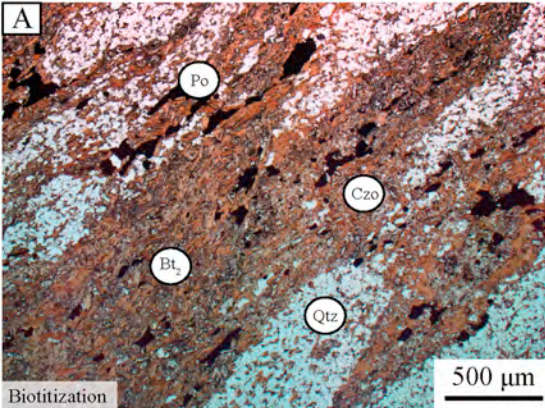
| Minerals | DK ₂ event / Prograde metamorphism and diorite emplacement | DK ₃ -DK ₄ events / Retrograde metamorphism during reactivation of D ₂ shearzones |
|---|---|--|
| Pyrrhotite ¹ Pyrite Chalcopyrite ¹ Arsenopyrite ¹ Invisible gold ? Electrum ^{2,3} Native gold ^{2,3} Tellurobismuthite | | |
| Biotite ^{1,2} Clinzoisite Diopside Tourmaline Muscovite Chlorite ³ Calcite | | |
| Mineralization styles | STAGE 1: <i>Stockwerk, replacements zone and dissemination</i> | STAGE 2: <i>Hydrothermal breccia, vein and veinlet and visible gold</i> |

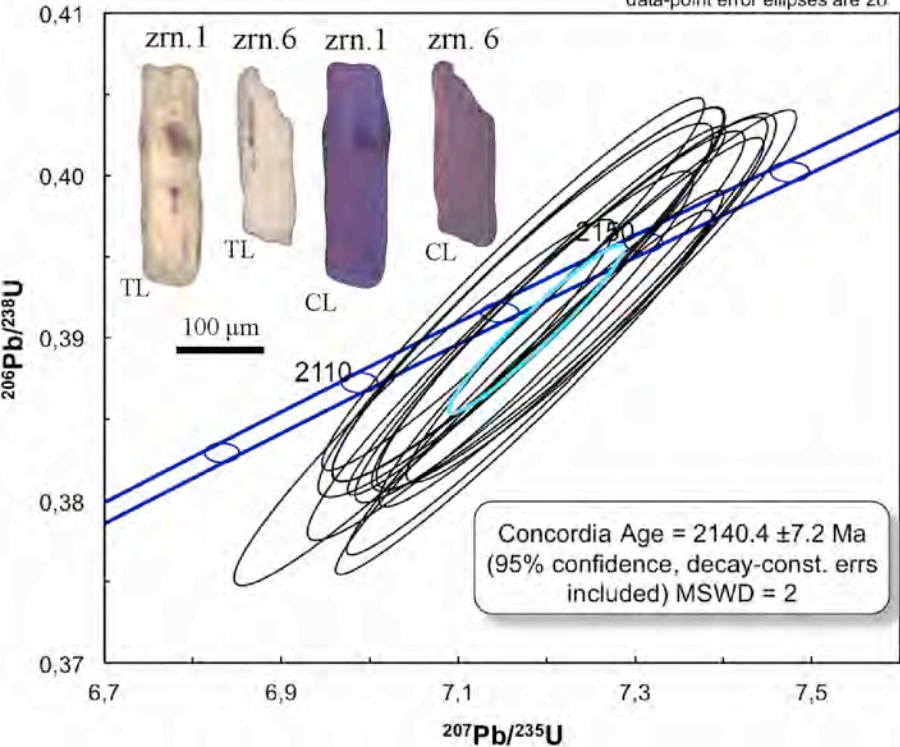
Major
 Minor
 Rare

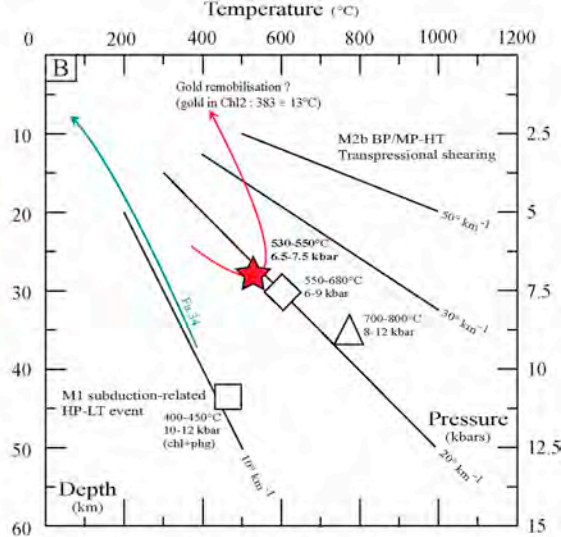
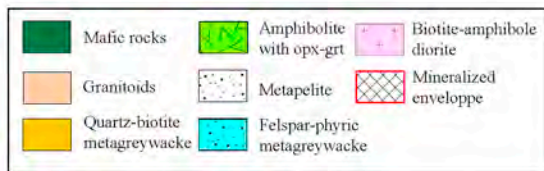
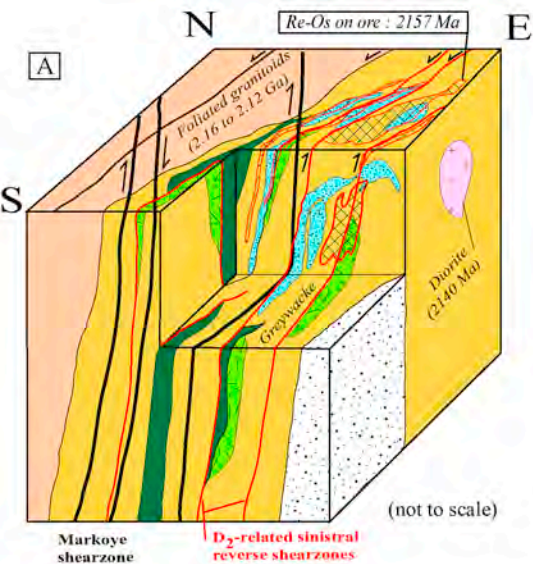
¹ mainly in aluminosilicate-bearing metapelites and quartz-biotite metagreywacke
² mainly in quartz-muscovite schist
³ mainly in metabasic rock











- M1 metamorphic event (Ganne et al., 2011)
- Melting at the granulite-amphibolite transition in northern Ghana (Block et al., 2015)
- Regional-scale amphibolite facies overprint in northern Ghana (Block et al., 2015)
- M2 metamorphic event (this study)

